Screened pseudo-charge repulsive potential in perturbed orbitals for band calculations by DFT+U

Bolong Huang

Department of Applied Biology and Chemical Technology, The Hong Kong Polytechnic University, Hung Hom, Kowloon, Hong Kong SAR, China

Email: bhuang@polyu.edu.hk

Abstract

The conventional linear response overestimates the U in DFT+U calculations for solids with fully occupied orbitals. Here, we demonstrate that the challenge comes from the incomplete cancellation of the electron-electron Coulomb repulsion energy under external perturbation. We applied the second charge response, denoted the "pseudo-charge" model, to offset such residue effects. Counteracting between these two charge response-induced Coulomb potentials, the U parameters are self-consistently obtained by fulfilling the conditions for minimizing the non-Koopmans energy. Moreover, the pseudo-charge-induced repulsive potential shows a screening behavior related to the orbital occupation and is potentially in compliance with the screened exact exchange-correlation of electrons. The resultant U parameters are self-consistent solutions for improved band structure calculations by DFT+U method. This work extends the validity of the linear response method to both partially and fully occupied orbitals and gives a reference for estimating the Hubbard U prior to other advanced methods. The U parameters were determined in a transferability test using both PBE and hybrid density functional methods, and the results showed that this method is independent of the functional. The electronic structures determined from the hybrid-DFT+U^{hybrid} approach are provided. Comparisons are also made with the recently developed self-consistent hybrid-DFT+U_w method.

Introduction

Describing the electron-electron interaction is key to solving electronic structures and understanding related properties of strongly correlated solids. The DFT+U method presents a simple way to describe electrons in semicore d or f orbitals in transition-metal or rare-earth compounds [1]. In this method, the Hubbard parameter U represents the on-site Coulomb repulsive potentials of localized d/f orbitals. The estimation of U by the conventional linear response (CLR) method under the density functional theory (DFT) framework has been widely used in solids with partially occupied orbitals (open shell) [2-10].

However, the CLR method is problematic for fully occupied orbitals (closed shell) and does not give a U in the physical range within 1 Ryd [10-16]. This discrepancy arises from the charge response (q) of perturbation being extremely underestimated by the Lagrange multiplier potential (α) in CLR calculations. As a result, the inverse of the response function, $U=(-\partial\alpha/\partial q)$, between localized electrons in closed shells is overestimated (i.e., $U\rightarrow\infty$ with the response $\Delta q\rightarrow 0$). These issues have been observed in many DFT+U calculations [15-17]. In addition, to address the Koopmans conditions in DFT+U calculations, Lany and Zunger have shown the importance of using this method to reflect the doping levels and electronic properties in the ZnO system [18, 19].

Using the approximation of Zunger and Freeman [20, 21], we updated the realistic electron addition energy in the current DFT+U theory scheme according to

$E(N+1)-E(N)=e_i(N)+\sum_i(U)+\Re_i(U)$, where $e_i(N)$ are the *i*th orbital eigenvalues of the N-electron system, $\sum_i(U)$ is the spurious self-energy of the *i*th orbital related to U, and $\Re_i(U)$ contributes the orbital wavefunction relaxation energy in excited states, which can be simplified as the difference between the relaxed and unrelaxed self-consistent excitation energy solutions in the DFT+U scheme. This contribution is treated as the relaxation-polarization of self-energy at the *i*th orbital mentioned above. $\sum_i(U)+\Re_i(U)$ has a nonlinear relationship with the U correction, as empirical tuning of U for correcting the orbital eigenvalues $e_i(N)$ led to a non-zero contribution of the $\sum_i(U)+\Re_i(U)$ such that the Janak theorem[22] has an inequality. Further theoretical works [18, 19, 23, 24] show that, by resembling the condition of generalized Koopmans' theorem (gKT), the term $\sum_i(U)+\Re_i(U)$ must be zero. Note that, solving this relation following gKT condition requires considerable mathematical effort. Therefore, in this work, we will choose a simplified model.

A considerable number of methods have been developed to study electronic structures. hybrid density functional methods are some of the most important methods. In these methods [25], part of the local DFT exchange is replaced with statically screened Hartree-Fock (HF) exchange, maintaining the original inter-electron correlation and effectively canceling the spurious self-interaction effects. This greatly improves the predicted electronic and magnetic properties. For instance, using the hybrid Perdew-Burke-Ernzerhof functional (PBE0) [26, 27] to simply replace a fraction (default portion=25%) of the local PBE [28] exchange has yielded reasonable band gaps [27, 29]. The Heyd-Scuseria-Ernzerhof (HSE03) functional [30-34], based on PBE0, includes a 25% screening of the long-range HF exchange by $\alpha_{HF}erf\left|\mu(\vec{r}-\vec{r}')\right|$ (note: α_{HF}=percentage of HF exchange). The screened exchange (sX) local density approximation functional (sX-LDA) [13, 35] replaces all LDA exchange with Thomas-Fermi-screened HF exchange and maintains the LDA correlation.

Semi-core fully occupied orbital-based solids (e.g., ZnO) have been studied by the HSE03, PBE0 and sX-LDA functionals [13, 36], and using these functionals obviously improves the electronic properties calculations. HSE03 with α_{HF} adjusted from 25% to 37.5% improves the band gap of ZnO to 3.43 eV (α_{HF}=37.5%) from 2.49 eV (α_{HF}=25%) [37]. Our collaborators showed that sX-LDA also provided a band gap of 3.41 eV when using a Thomas-Screening Length (k_{TF}) of 2.27 A^{-1} (or 1.2 $Bohr^{-1}$) [36]. Recent work has shown that combining HSE with the many-body GW method (HSE+GW) with α_{HF}=25% improves the band gap to 3.34 eV from 2.34 eV by plain HSE06 (α_{HF}=25%) [38]. This suggests that short-range electron-electron exchange-correlation contributions in hybrid density functional methods could be further improved.

More importantly, hybrid density functional methods, as efficient approaches with lower computational costs than GW, can be tuned in a systematic manner to obtain more accurate band gaps and other electronic properties. It should be introduced that the significance of non-empirical range-separated hybrid-functional development has been recently addressed [39-43]. For instance, the dielectric-dependent hybrid density functional method such as DDH self-consistently determined the fraction of HF exchange based on physically meaningful parameters valid for both solids and molecules (finite system) within the generalized Kohn-Sham framework [39, 40]. Further examining the completeness of the hybrid-DFT+U method, Ivady and Gali et al. made a remarkable development [44, 45]. With an insightful derivation, they were the first to note that some range-separated hybrid density functional methods, such as HSE06, do not fulfill the generalized Koopmans theorem (gKT)

for describing the defect states of selected solid systems [44]. Furthermore, their following theoretical work supports that the relationship between hybrid-DFT and DFT+U justifiably exists under the fully localized limit (FLL) approximation [45]. Such a relationship advantageously maintains the same on-site occupation matrix for each, which was previously used in the works of Cococioni et al. [9, 46]. In this method, the original Hubbard U_{eff} potential is replaced by a multiplicative operator of α_{HF} and Slater integrals (F^0 and J^0) [44, 45]. Computations on localized orbitals are benefited, in that the contribution to the total energy by hybrid-DFT (e.g., PBE0) in terms of additional orbital-dependent potential corresponds to the Hubbard U correction used in DFT+U.

Hybrid-functional calculations have been used to fit U [47, 48], but still at high cost. It is ineffective to predict the physical and chemical properties of newly synthesized and novel solid materials [49, 50]. Moreover, the simple combination of HSE+(Hubbard U) for band gap calculations has yet to be widely tested [51, 52], because α_{HF}, ω, k_{TF}, and U must be determined globally. Previous work has shown that the self-consistent CLR process leads to a singularity in solids with a fully occupied 4f shell [53]. The singularity may arise from incomplete cancellation of the electron-electron Coulomb repulsion energy (i.e., E_H, Hartree component of the orbitals) under perturbation, as the on-site *Hartree energy* (E_H) component has been found to be precisely cancelled in bare DFT+U calculations [1, 54, 55], where the form is often given as $E_H=(1/2)UN^2$ under rotational invariance [55]. Moreover, the determination of U is still far from being well understood and resolved, especially at the electronic level and with functional choice.

Therefore, we argue that external perturbation in the CLR method gives rise to an incompletely cancelled Hartree energy residue within a constrained volume of the periodic supercell, acting as the on-site non-Koopmans energy term E_{NK} in $E=E^{DFT}+E_{NK}$. To illustrate a method for minimizing E_{NK} to fulfill the general Koopmans conditions, we start with DFT+U calculations and apply a complementary reference to further develop the calculation. Our method works regardless of the choice of XC functional or valence pseudopotential (PP), especially for fully occupied shells, and will allow the future study of their electronic structures, optical properties, thermodynamics and optical transition levels.

Calculation Method and Setting

1. The conventional linear response

The CLR method is popular for calculations on open-shell transition metals (e.g., $3d^1$-$3d^9$) and rare earth elements ($4f^1$-$4f^{13}$) [2-10].]. In this method, an on-site Lagrange-type multiplier (α_I, called the perturbation potential) is projected on the charge occupation of the designated orbital, as shown in Eq. (1). U is estimated from the difference in the first derivative perturbation potential over the charge response under external input perturbation both before and after Kohn-Sham minimization [9], in the framework of Janak's theorem [56]. The formalism of the CLR method imbedded in the bare DFT total energy functional is given by

$$
\begin{aligned}
&E[n,q]=E^{DFT}[n]+E^{ext}=E^{DFT}[n]+\sum_I \alpha_I[n_I-q_I]=T[n]+E_{i-e}[n]+E_{ee}[n]+\sum_I \alpha_I[n_I-q_I]\\
&n_I=\sum_{\sigma,m} n^{\sigma}_{mm'}=\sum_{\sigma}\sum_{n,\mathbf{k}} f^{\sigma}_{n,\mathbf{k}}\left\langle \psi^{\sigma}_{n\mathbf{k}}\middle| P^I\middle|\psi^{\sigma}_{n\mathbf{k}}\right\rangle, \quad \left(0\le f^{\sigma}_{n,\mathbf{k}}\le 1\right) \qquad , (1)\\
&P^I=\sum_m P^I_{mm'}=\sum_m \left|\phi^I_m\right\rangle\left\langle\phi^I_{m'}\right|
\end{aligned}
$$

The term n_I is transformed from the non-interacting charge density under a single-electron model, P^I is the projector of localized states of an atom at site I, and $f_{n,\mathbf{k}}^{\sigma}$ is the occupation number, which follows $0 \le f_{n,\mathbf{k}}^{\sigma} \le 1$ for single-electron Kohn-Sham orbitals. From the CLR method introduced by Cococcioni and de Gironcoli [9], the Hubbard parameter is yielded from the *negative* curvature of the total energy $E[q_I]$, which is an output of the negative second-order derivative of constrained total energy. The effective Hubbard U is obtained from the following relationship:

$$U_{scf} = U_{out} = U_{out}^{KS} - U_{out}^{initial} = \frac{\partial^2 E[q_I]^{initial}}{\partial q_I^2} - \frac{\partial^2 E[q_I]^{KS}}{\partial q_I^2} \tag{2}$$

where the subtraction works to mutually extract the unphysical part that is retained both before and after KS minimization of the total energy functional, as suggested by Cococcioni and de Gironcoli [9]. With this method, the self-consistent U parameter (U_{scf}) is treated by the output of the CLR calculation (U_{out}) in the above Eq. (2). A similar discussion was also provided by Pickett et al. [8].

However, as shown in Table 1, the perturbed charge is found to persistently vanish upon on-site perturbation α_I of the frozen fully occupied d/f shell. This results in an overestimation of the inverse of the response function, $\chi^{-1}=\partial\alpha/\partial n$ (to yield U), between localized electrons in a closed shell (e.g., χ^{-1} with the response $\chi \to 0$), as reported previously [15-17]. Thus, U is overestimated by the CLR method in the case of fully occupied orbitals (Table 2).

2. The Non-Koopmans energy and electron-electron repulsion energy

In Eq. (1), $T[n]$ and $E_{i\text{-}e}[n]$ are the kinetic energy and ion-electron interaction energy, respectively. For d/f electrons there are three nonvanishing Slater's integrals F^0, F^2, and F^4 that can be expressed with only two parameters,

$$\begin{aligned} F^0 &= \frac{1}{(2l+1)^2}\sum_{m,m'} F^0_{mm'} = \frac{1}{(2l+1)^2}\sum_{m,m'}\langle mm'|v_{ee}|mm'\rangle \\ J^0 &= \frac{1}{2l(2l+1)}\sum_{m\neq m',m'}\langle mm'|v_{ee}|m'm\rangle = \frac{F^2+F^4}{14} \end{aligned} \tag{3a}$$

Where the ratio has $F^4/F^2 \approx 0.625$. The electron-electron interaction in localized orbitals by the fully localized-limit (FLL) approximation is described by [45]

$$E_{ee}[n] = E_{ee}^{DFT}[n^{\sigma}] = \frac{F^0}{2}n^2 - \frac{F^0 - J^0}{2}n - \frac{J^0}{2}\sum_{\sigma}(n^{\sigma})^2, \tag{3b}$$

Here, F^0 and J^0 are the Slater integrals, and σ is the spin index. Actually, the parameters of Hubbard U and the Stoner J are the screened value of F^0 and J^0, respectively. The term $(F^0/2)n^2$ is the electron-electron static Coulomb repulsion energy, also called the *Hartree energy*, which equals the Coulombic self-energy of a given charge occupation *n.* Similarly, in the mean-field (MF) limit, this term can also be approximated by the rotational invariance to yield $E_H=(U/2)n^2$, and $E_{ee}[n]$ is described by

$$E_{ee}[n]=\frac{U}{2}n^2-\frac{U-J}{2}\sum_{m,\sigma}n_{m,\sigma}^2-\frac{J}{2}\sum_{\sigma}(n^{\sigma})^2, \tag{4}$$

Considering that the electron-electron interaction term has now been updated by the change in the on-site orbital occupations from n_I to q_I by external linear perturbation, the CLR total energy functional is rewritten as follows:

$$E[n,q(\alpha)_I,\alpha_I]=\{T[q]+E_{i-e}[q]+E_{ee}[q]\}+\{E_{ee}[n]-E_{ee}[q]\}+\sum_I\alpha_I[n_I-q_I], \tag{5}$$

The first bracket already fulfills the gKT conditions, and the differences of $T[q]$ and $E_{i\text{-}e}[q]$ can be neglected. Furthermore, $E_{ee}[q]$ fully considers the electron-electron interaction in compliance with the HF approximation [45]. Therefore, the task is to minimize the sum of the remaining terms, which are taken as the non-Koopmans energy (E_{NK}), $E_{total}=E^{DFT}[q]+E_{NK}(q_I,\alpha_I)$. Thus, the rotational invariant E_{NK} is written as

$$E_{NK}=\sum_I\{\alpha_I(n_I-q_I)+\frac{\sigma_I}{2}[n_I^2-q_I^2]\}\cong\sum_I\{\alpha_I(n_I-q_I)+\sigma_I[(n_I-q_I)]q_I\}, \tag{6}$$

To maintain the gKT condition of self-consistency, the constrained conditions follows:

$$\begin{aligned}&E_{NK}\approx 0\\&\lim_{q\to n}(\nabla_q E)=\lim_{q\to n}(V_{NK})\to 0\\&\nabla_q^2E=U_{NK}>0\end{aligned} \tag{7}$$

Because the charge occupation follows $q_I\approx n_I$ for fully occupied orbitals when CLR is applied (Table 1), we simply use an on-site multiplicative potential operator σ_I instead, which will be defined in the following text. In addition, $\sigma_I n_I$ is simply replaced with a notation of an external input parameter $U_{in,I}$ for a flexible interval setting, which is used as an iteration step-size to search for the minimum (i.e., quantitatively, $U_{in,I}(q_I)=\sigma_I q_I$). Considering that CLR induces a small external potential input $|\alpha_I|\ll 1$ (i.e., $q_I\to n_I$), the magnitude of E_{NK} approaches zero. Thus, to fulfill the Koopmans condition by $\nabla_q E_{NK}$ and $\nabla_q^2E_{NK}$ is the criterion for searching the U. We now verify that it is a minimum: the total differential form of $E_{NK}=E_{NK}(q_I,\alpha_I)$ is $dE_{NK}=\frac{\partial E}{\partial q_I}dq_I+\frac{\partial E}{\partial\alpha_I}d\alpha_I$, and thus the q-gradient of E_{NK} ($\nabla_q=\frac{d}{dq}$) is

$$\nabla_q E_{NK}=\frac{\partial E}{\partial q_I}+\frac{\partial\alpha_I}{\partial q_I}\frac{\partial E}{\partial\alpha_I}. \tag{8}$$

After the Kohn-Sham self-consistent iterations of Eq. (4), the solution of the total energy functional is

$$E=\min_{n(\mathbf{r}),q(\alpha_I)_I,\alpha_I}\left\{E_{KS}^{DFT+U}[n]+\sum_I\sigma_I^{KS}\left[n_I-q(\alpha_I)_I\right]^{KS}q(\alpha_I)_I^{KS}+\sum_I\alpha_I^{KS}\left[n_I-q(\alpha_I)_I\right]^{KS}\right\} \tag{9}$$

Applying the Hubbard U to the quadratic term in $E[n,q(\alpha_I),\alpha_I]$ in total energy of the system gives the on-site chemical potentials of the perturbed orbital occupation in the following Eq. (10) and the orbital perturbation imported pseudo-charge in the following Eq. (11):

$$\begin{cases}\dfrac{\partial E[n,q(\alpha)_I,\alpha_I]_U^{initial}}{\partial q(\alpha)_I}=-\left[(\sigma_I n_I)^{initial}+\alpha_I^{initial}\right]=-\left(U_{in,i}^{initial}+\alpha_I^{initial}\right)\\ \dfrac{\partial E[n,q(\alpha)_I,\alpha_I]_U^{KS}}{\partial q(\alpha)_I}=-\left[(\sigma_I n_I)^{KS}+\alpha_I^{KS}\right]=-\left(U_{in,I}^{KS}+\alpha_I^{KS}\right)\end{cases} \tag{10}$$

$$\begin{cases}\dfrac{\partial E[n,q(\alpha)_I,\alpha_I]_U^{initia}}{\partial\alpha_I}=n_I^{initial}-q(\alpha_I)_I^{initial}\cong\Delta n_I^{initial}\cong\left(\dfrac{\partial n_I}{\partial\alpha_I}\alpha_I\right)^{initial}=\left(-\dfrac{\alpha_I}{U_{in,I}}\right)^{initial}\\ \dfrac{\partial E[n,q(\alpha)_I,\alpha_I]_U^{KS}}{\partial\alpha_I}=n_I^{KS}-q(\alpha_I)_I^{KS}\cong\Delta n_I^{KS}\cong\left(\dfrac{\partial n_I}{\partial\alpha_I}\alpha_I\right)^{KS}=\left(-\dfrac{\alpha_I}{U_{in,I}}\right)^{KS}\end{cases} \tag{11}$$

In our previous work [53], we showed that the perturbed charge q_I can also be derived by the Maclaurin series (a Taylor expansion at the zero point) $n_I=q_I+\dfrac{\partial q_I}{\partial\alpha_I}\alpha_I+O(\alpha_I^2)$. Then, $\left(\dfrac{\partial E}{\partial\alpha_I}\right)=n_I-q_I\cong\dfrac{\partial q_I}{\partial\alpha_I}\alpha_I=-\dfrac{\alpha_I}{U_I}$ or $\dfrac{\partial E}{\partial\alpha}=\dfrac{\partial E}{\partial q(\alpha)}\dfrac{\partial q(\alpha)}{\partial\alpha}\cong-\dfrac{\alpha}{U_{in,I}}$. In the linear regime, $-\dfrac{\partial q_I}{\partial\alpha_I}=\dfrac{1}{U_I}$ is valid [8, 9]. Upon a small charge perturbation by the external potential $|\alpha_I|<<1$, $q_I\approx n_I$. Then, the first derivative of E_{NK} is updated to

$$\nabla_q E_{NK}=\left(\frac{\partial E}{\partial q}-U\frac{\partial E}{\partial\alpha}\right)=-\sigma_I n_I=-U_{in} \tag{12}$$

Only when $U_{in}\to 0$ does E_{NK} have an extremum. Thus, the conventional linear response, which considers q_I as the only independent variable (i.e., $E_{NK}=E_{NK}(q_I)$), cannot ensure that the global minimum of E_{NK} is zero, which means $\nabla_{q_I}^2E(n_I-q_I)=-U_I\delta(n_I-q_I)$.

The second-order gradient is further shown as follows:

$$\nabla_q^2E_{NK}=\frac{\partial^2E}{\partial q_I^2}+\frac{\partial\alpha_I}{\partial q_I}\frac{\partial}{\partial q_I}\left(\frac{\partial E}{\partial\alpha_I}\right)+\frac{\partial^2\alpha_I}{\partial q_I^2}\frac{\partial E}{\partial\alpha_I} \tag{13}$$

3. Pseudo-charge induced two-way crossover linear response

To guarantee that this extremum is the minimum value of E_{NK}, $\nabla_q^2 E_{NK}$ should be always positive. However, CLR only considers the charge q response by introduction of α_I without showing the pseudo-charge when the incompletely cancelled electron-electron Coulomb potential energy is further varied. Here, we simply reflect the pseudo-charge contribution scaled by α_I and U_{in}. The α_a is used to reflect the pseudo-charge induced by the external potential perturbation (α_I) on the specific orbital with quantity scaled by (α_I/U_{in}) under standard PBE+U_{in} calculations. The α_b is for describing the potential contributed by such pseudo-charge. Thus, two sets of perturbation systems with two different charge responses exist. The two Lagrange-type potential multipliers are shown as follows:

$$\text{set} \quad \begin{cases} \alpha_a = a \cdot \alpha_I = \dfrac{\alpha_I}{U_{in}} \cdot a_0 \\ \alpha_b = U_{in} + \alpha_I \end{cases} \tag{14}$$

From the above, we give the unit potential as $a_0 = 1\ eV$ to maintain the dimension. Then, we have two different Lagrange multipliers with the relationship of

$$\alpha_a \cdot \alpha_b = a_0 \cdot \alpha_I + \frac{\alpha_I^2}{U_{in}} \cong a_0 \cdot \alpha_I \tag{15}$$

We set two perturbations in Eq. (14) because we cannot be certain about the realistic non-linear relationship between the input Hubbard U parameter U_{in} and the occupancies of the orbitals. Therefore, we recast the linear response to calculate U_{scf} by the potential energy response instead of the charge occupancy because the charge occupancy response for closed shells is less effective under both the meanfield (MF) and atomic-limit (AL) approximations. Re-distributing the two different Lagrange potential multipliers in the total energy functional gives the following:

$$\begin{cases} E\left[\{q_I(a)\},\alpha_a\right] = \min\limits_{n(r),\alpha_a}\left\{E^{DFT+U}[n] + \sum\limits_I \alpha_a\left[n_I - q_I(\alpha_a)\right]\right\} \\ E^{KS}\left[\{q_I(a)\},\alpha_a\right] = \min\limits_{n(r),\alpha_a}\left\{E_{KS}^{DFT+U}[n] + \sum\limits_I \alpha_a^{KS}\left[n_I - q_I^{KS}(\alpha_a)\right]\right\} \end{cases} \tag{16}$$

$$\begin{cases} E\left[\{q_I(a)\},\alpha_b\right] = \min\limits_{n(r),\alpha_b}\left\{E^{DFT}[n] + \sum\limits_I \alpha_b\left[n_I - q_I(\alpha_b)\right]\right\} \\ E^{KS}\left[\{q_I(a)\},\alpha_b\right] = \min\limits_{n(r),\alpha_b}\left\{E_{KS}^{DFT}[n] + \sum\limits_I \alpha_b^{KS}\left[n_I - q_I^{KS}(\alpha_b)\right]\right\} \end{cases} \tag{17}$$

Referring to the work of Kulik, Cococcioni and co-workers [57], we can easily re-write the output U parameter from Eq. (16) in the form of U_{out1}. For U_{out2} generated from Eq. (17), we consider a more general description from Eq. (2), giving

$$U_{out1} = -\left(\frac{\partial \alpha_I}{\partial q(a)} - \frac{\partial \alpha_I^{KS}}{\partial q(a)^{KS}}\right) = -\left(\frac{\partial \alpha_a}{\partial q(a)} - \frac{\partial \alpha_a^{KS}}{\partial q(a)^{KS}}\right) \cdot \left(\frac{U_{in}}{a_0}\right) = -\left(\frac{U_{in}}{a_0}\right)\left(U_{scf1}(U_{in}) - \frac{U_{in}}{m}\right) \tag{18}$$

$$U_{out2} = -\left(\frac{\partial \alpha_I}{\partial q(b)} - \frac{\partial \alpha_I^{KS}}{\partial q(b)^{KS}} \right) \tag{19}$$

where m is the linear order form of the effective degeneracy introduced in the CLR method $m = 1/\sum_i (a_i^I)^2$ and $\sum_i a_i^l = 1$. In a fully occupied shell, $m = 1$. Considering Eqs. (8) to (11), the resultant U parameter has a relationship between Eq. (19) and Eq. (2), and the presentation without considering "initial" and "KS" is simplified and is given as follows:

$$\begin{aligned} U_{out2}{}' = U_{scf} &= \frac{\partial^2 E[q_I]^{initial}}{\partial q_I^2} - \frac{\partial^2 E[q_I]^{KS}}{\partial q_I^2} = \left(\frac{\partial \alpha_b}{\partial q(b)} - \frac{\partial \alpha_b^{KS}}{\partial q(b)^{KS}} \right) \\ &= \left(\frac{\partial U_{in}{}^{initial}}{\partial q_I} - \frac{\partial U_{in}{}^{KS}}{\partial q_I} \right) + \left(\frac{\partial \alpha_I}{\partial q(b)} - \frac{\partial \alpha_I^{KS}}{\partial q(b)^{KS}} \right) = -\frac{\partial U_{in}}{\partial q_I}\Big|_{KS}^{initial} + U_{out2} \end{aligned} \tag{20}$$

Thus, $U_{out2} = \frac{\partial U_{in}}{\partial q_I}\Big|_{KS}^{initial} + U_{scf}$ (21)

From Eqs. (18) to (21), we see that the U_{scf} vs U_{in} behavior is still unknown, while U_{scf} is calculated based on U_{out1} (or U_{out2}) and U_{in} in Eq. (21). Therefore, any one of them cannot solely determine U_{scf}. When the two different charge response system-induced Hubbard parameter outputs are equivalent, U_{scf} is thus determined by an input U_{in} when the two output calculated U values have U_{out2}-U_{out1}=0. Therefore, the relationship of U_{scf} and U_{in} can be described by

$$U_{scf} = \frac{\left(\frac{U_{in}}{m} \right) - \left(\frac{a_0}{U_{in}} \right)\left(\frac{\partial U_{in}}{\partial q_I} \right)}{1 + \left(\frac{a_0}{U_{in}} \right)} \tag{22}$$

We have already given the behavior of U_{out1} and U_{out2} related to U_{in} within fully filled or non-fully filled shells with different maximum angular momentums, as shown in Figure 1. Specifically, we have seen that U_{out2} almost demonstrates a linear relationship with a relatively small input U_{in}, shown as

$$U_{out2} = kU_{in} + U_{scf} \ , (k < 0) \tag{23}$$

where the k denotes a constant slope of approximated linear relationship. Thus, considering Eqs. (21) and (23) and recalling the replacement above ($U_{in,I}(q_I) = \sigma_I q_I$), the relationship is updated as follows:

$\frac{\partial U_{in}}{\partial q_I}\Big|_{KS}^{initial} = kU_{in}$, or $U_{in} = [U_{in}(0)]\exp[kq_I]$, ($U_{in}(0)$ is the bare chemical potentials on the orbitals when response charge q_I=0.) (24)

Replacing $\frac{\partial U_{in}}{\partial q_I}$ with kU_{in} in Eq. (22) results in

$$U_{scf} = \frac{\left(\frac{U_{in}}{m}\right) - a_0 k}{1 + \left(\frac{a_0}{U_{in}}\right)} \tag{25}$$

Thus, the multiplicative potential operator induced by the pseudo-charge σ_I is

$$\sigma_I = \frac{U_{in}(0)}{q_I} \exp[kq_I], (k < 0) \tag{26}$$

Here, $[n_I\text{-}q_I]$ is close to zero, as shown in Table 1. Thus, we apply the approximation $n_I = q_I$. By the approximated presentation in Eq. (26), the process of U_{scf} on the closed shell solid orbitals by way of the U_{in} response is self-consistent and maintains the gKT. Furthermore, the multiplicative potential operator turns out to be asymptotically converged to zero (i.e. an exponentially decaying function vanishes at infinity). It can largely reflect the on-site screening potential behavior when the external Lagrange-type potential perturbation α_I is induced. The magnitude of σ_I is an infinitesimal screening potential operator when n$\approx$ 10 for a d orbital or n$\approx$14 for an f orbital. This addresses the pseudo-charge induced by the external perturbing potential, which is self-consistently yielded (Eq. (26)) to fulfill the gKT conditions. The relationship between the on-site σ_I and occupation response q_I is shown in Figure 2.

To re-address the singularity problem from CLR method, we integrate the Eq. (24) from 0 to $Q_I=[n_I\text{-}q_I]$ instead of from 0 to q_I and re-write the Eq. (26) with a updated form as $U_{in}(Q_I) = U_{in}(0)\exp[k(Q_I)]$, where k<0. In a small range of perturbation, the magnitude of external perturbation introduced from CLR is from 0 to an updated value of $\alpha_I \approx U_{in}(Q_I)$, because the charge response is $n_I \approx q_I$ in closed-shell solids.

The CLR method claimed that the self-consistently yielded U parameter is given by the second derivative of total energy functional which is also the first derivative of such on-site perturbation α_I. Thus, the U is perceived from this manner is approximately shown by $U_{output} \cong \frac{U_{in}(0)\exp[k(n_I - q_I)]}{n_I - q_I}$, which is a similar trend of the physical Dirac-function: $U_{in}(0)\delta(n_I - q_I)$, when $n_I \to q_I$. Therefore, we recall the singularity issue of the conventional charge response-based U determination on closed-shell orbitals. The on-site potential perturbation is largely screened at full charge occupation, which is why the conventional single-way linear response fails in closed-shell orbital-based solids, as the on-site potential perturbation is almost mutually offset with the full charge occupation.

Recalling that the minimization of E_{NK} is always constrained to zero, the conditions shown in Eq. (7) show that $\lim_{q\to n}\frac{\partial\sigma_I}{\partial q_I}\cong 0$ in Figure 2. Meanwhile, the second-order q-gradient of E_{NK} is updated as follows:

$$\nabla_q^2 E_{NK} = U_{out2} - U_{out1} - \frac{\partial U_{in}}{\partial q_I} - \frac{\partial U_{in}}{\partial q_I}\frac{\alpha_I}{U_I} = \Delta_I - k\left(U_{in} + \alpha_I\right) \cong \Delta_I - kU_{in} > 0\,, \tag{27}$$

Note that $k < 0$. For charge fully distributed in orbitals, Δ_I is found to be zero which means a crossover or tangent point, while it is positive in partially occupied orbitals. The crossover point of Figure 1 validates $(U_{out2} - U_{out1})_I = 0$ based on the condition of Eq. (27). Thus, E_{NK} is now confirmed in this work to always have a minimum, and our method provides a process for minimizing E_{NK}.

4. Computational Setting

This computational method is actualized by a parallel Python execution integrated with two CASTEP development codes, in which the method was preliminary implemented [53]. It operates with simultaneous two-way crossover linear response calculations. As the following test materials are mostly oxides, the norm-conserving PPs are generated using the OPIUM code in the Kleinman-Bylander projector form [58], and the non-linear partial core correction [59] and a scalar relativistic averaging scheme [60] are used to treat the spin-orbital coupling effect. The RRKJ method is chosen for the optimization of the PPs [61]. The PBE functional is chosen for the rotationally invariant DFT+U calculations [62] with a kinetic cutoff energy of 750 eV, with the valence electron states expressed in a plane-wave basis set. The ensemble DFT (EDFT) method of Marzari et al. [63] is used for convergence. Reciprocal space integration is performed using *k*-point grids with a separation of 0.04 ($Å^{-1}$), and the total energy is converged to less than 5.0×10^{-7} eV per atom. The Hellmann-Feynman forces on the atom were converged to less than 0.01 eV/Å. It is necessary to consider the computational cost. If the efficiency of the conventional DFT+U algorithm is *~O(NlogN)*, the calculation cost for this method is approximately $O(NlogN)<\tau<O(N^2logN)$, as it will do a further linear response calculation based on each $U_{in,I}$ given in Eq. (9). The above *O* denotes the computational time-scale of the given algorithm.

For the cell models we used for calculation tests, we used the unit cell of wurtzite (WZ) and primitive cell zincblend (ZB) ZnS lattices, which are 4 and 2 atoms in a cell, respectively. The primitive cell of kesterite (KS) and unit cell of wurtzite (WZ) phase of Cu_2ZnSnS_4 (CZTS) have been also taken into account for the closed-shell solids calculations for discussion. The ground state optimized cell lattice parameters for ZnO, ZnS and CZTS have been shown in Table 3 with comparison to the experimental values. Their cells contain 8 atoms and 16 atoms respectively. For the ZnO and ZnS calculations, k-point sampling with 9×9×6 and 10×10×10 in reciprocal grids have been chosen respectively for PBE+U calculations, while 4×4×3 grid for sX-LDA computational test on ZnO. For the primitive cells of Cr_2O_3 and $Co_3V_2O_8$ structures, k-point sampling grids are chosen as 6×6×6 and 5×5×3 respectively for PBE+U calculations.

Results and discussion

1. Band structures for closed-shell solids

Here, we describe some comparisons of the experimental data with the DFT+U calculation results, based on suggested U. Figure 3 (a) and (b) show a comparison of the band structures of WZ-ZnO and ZB- ZnS regarding movement of the $3d^{10}$ level for Zn in the relevant oxide and sulfide. The 3d level for ZnO is broader than that for ZnS and remains as high as -7.5 eV (VBM = 0 eV); however, it is -10.7 eV in ZnS. The 3d level of ZnO is remarkably similar to the reported experimental value of -7.5 eV determined using high-resolution resonant angle-resolved photoemission spectroscopy (ARPES) [64]. In addition, the s levels of the S sites in ZnS are shifted even higher than the 3d level of Zn, indicating a hybridization trend of the s-p orbitals of S. The s band in ZnS overlaps the 3d band at the Γ of the first Brillouin zone (BZ). This result shows a relatively strong p-d entanglement in ZnO compared to that in ZnS because the 3d level moves deeper (to 3.2 eV) in the latter material.

Figure 3 (c) and (d) provide the electronic structures of copper-zinc-tin-sulfides (i.e. Cu_2ZnSnS_4 or CZTS) in both kesterite phase (KS) and hexagonal wurtzite phase (WZ) like lattices, showing that they both have direct band gaps. The latter was recently successfully synthesized by Li et al. [65]. We see that the Cu 3d levels are similarly located at the top of the valence band in both KS and hexagonal WZ-like lattices. The 3p levels of S are hidden in the middle between the t_{2g} levels of the 3d orbitals of Cu and Zn, where the 3d of Zn remains at approximately -10 eV. The band gaps are determined to be 1.404 eV and 1.440 eV for the KS and WZ-like lattices, respectively, which are consistent with the experimental values of 1.4~1.5 eV.

We further demonstrate the difference of the PBE and PBE+U calculations in the electronic DOSs of wz-ZnO, zb-ZnS, KS-CZTS, and WZ-CZTS respectively, shown in Figure 3 (e)-(i). Details of the comparison with standard PBE+U calculations are provided in from Figure S1to Figure S3 in the supplemental information.

In Figure 3 (e), we see that the 3d occupied levels of Zn in wz-ZnO by PBE+U_{scf} calculations has down shifted with about 3.5 eV lower than the calculations by plain PBE. The starting positions of 3d levels of Zn are shown at 7.53 eV below the valence band maximum (VBM, 0 eV) by our PBE+U_{scf} calculations. The PBE calculations vastly underestimated not just in the band gap width but also the 3d levels, as it is showing an over too strong hybridization of Zn 3d and O 2p orbitals in Figure 4 (e). Meanwhile, the band gap width has increased from 1.035 eV to 3.441 eV much closer to the experimental value[66, 67], and also reach the nearly the same level that achieved by tuned U from the successful work by Ma et al [68], and the comparison is shown in Figure 3 (i). In the calculations, we chose the non-linear core corrected (NLCC) pseudopotentials based on our previous method[69], and find it also improved the formation enthalpy of the system, which is from -2.93 eV to -3.20 eV by plain PBE without NLCC and with NLCC respectively. Based on the U_{scf} correction, the formation enthalpy has also been improved to be -3.70 eV in agreement with experimental data of -3.63 eV [66, 67]. The error of lattice parameter optimization is reduced by our PBE+U_{scf} calculations compared with the ones in PBE. The overall improvements of U_{scf} and the NLCC pseudopotential have been shown in Table 4 focus on ZnO as an example, and our calculations are also have comparable accuracy levels to the screened exchange (sX) calculations done one of our previous collaborators, Robertson et al [13, 14, 36].

In Figure 3 (f), the starting positions of 3d occupied orbital levels of Zn are updated from 5.2 eV below the VBM downward to the 8.0 eV below the VBM, improved by 2.8 eV from

PBE to PBE+U_{scf} calculations. From our PBE+U_{scf} calculation, the dominant peak of 3d orbitals of ZnS in DOS is staying at 10.7 eV below the VBM. We also see that the 3d level of Zn in ZnS is relatively deeper than in the ZnO. The band gap width has also increased from 2.12 eV to 3.85 eV accordingly, with improvement of 1.7 eV and much closer to experimental optical fundamental gap of 3.8 eV.

In Figure 3 (g) and (h), we further on a comparison of CZTS system by PBE and PBE+U_{scf} calculations in kesterite (KS) and wurtzite (WZ) phases respectively. We see that the anti-bonding state of Sn is dominated by 5p orbitals, which is up-shifted from 0.17 eV to 1.40 eV in kesterite and from 0.04 eV to 1.44 eV in wurtzite phase. The energy intervals between the Cu 3d and Sn 5p levels are actually the optical band gap measured experimentally. The band gap thus is improved by 1.2 eV~1.4 eV. Experimentally, the band gap of CZTS is reported to be 1.4~1.5 eV. The Cu 3d level in CZTS system is updated with about 0.6 eV in KS phase and 0.5 eV in WZ phase, and both downward shifting away from VBM. The S 3p orbital levels are also showing similar magnitude of shifting from PBE updated to PBE+U_{scf} calculations. The $3d^{10}$ levels of Zn sites within KS and WZ phases are showing an updated level with shifting of 2.0 eV and 1.9 eV respectively toward to a deeper range lower from VBM.

2. Band structure for open-shell (corundum Cr_2O_3)

In this work, we choose the Cr_2O_3 system to validate the method on a 3d open-shell system. Cr_2O_3 is an important functional material in the study of magnetoelectric effects [70], due to its localized 3d electrons. It has been reported that Cr_2O_3 is an intermediate charge transfer (CT)-Mott-Hubbard (MH) insulator [71] with a wide band gap in the anti-ferromagnetic (AFM) phase. The most stable G-type AFM phase is the ground state at 0 K, as reported by both experiments and theoretical calculations [72, 73].

Experimental measurements give its band gap in a general range of 3.0 eV to 3.5 eV. Optical absorption measurements show an optical fundamental band gap of 3.3 eV [72, 73], while photoemission experiments report that the value is approximately 3.4-3.5 eV [74]. However, the band gap is also influenced by the synthetic and processing techniques, and polycrystalline Cr_2O_3 made by chemical vapor deposition (CVD) has a band gap of 2.98-3.09 eV, as indicated by its optical transmission spectrum [75].

In calculations from other groups, the DFT-LDA/GGA level gives a band gap of 1.5 eV, which is vastly underestimated [72, 73]. DFT+U based on the method of Mosey and Carter gives an improved band gap of 2.9 eV, based on an unrestricted Hartree-Fock (UHF) method, while the Hubbard U parameters are different by 3.2 eV and 7.7 eV. One of our previous collaborators systematically investigated the electronic structure by the sX method and obtained a band gap of 3.31 eV [76], close to the optical absorption value [72]. However, the sX calculation finds a magnetic moment (μ_B) for Cr in the G-type AFM phase that is still less than the experimental value of 3.8 μ_B [72, 73]. We further noted that this may arise from another dominant error in the PPs for magnetic transition metals or heavy lanthanide ions due to the core-valence charge density overlap [69]. This overlap-induced error can be reduced through modeled partial core corrections within the framework of non-linear core corrections [69].

In our calculations, we chose the primitive cell of Cr_2O_3 in the corundum lattice with the symmetry space group *R3c* and a G-type AFM arrangement of the Cr^{3+} net spins along the <111> direction. Based on our method, the Hubbard parameter is 4.90 eV for the 3d orbitals

of the Cr^{3+} sites and 6.16 eV for the 2p orbitals of the O^{2-} sites. These Hubbard parameters are obtained from Figure 4. Carter et al. used the molecular orbital (MO) method based on the UHF scheme to determine the values, which are 7.7 eV [77] and 3.2 eV [78] with different basis set methods and techniques. These values evidently deviate from the experimental estimated value of 4.0 eV. However, according to the asymptotic empirical tuning, the LDA/GGA+U method gives a reasonable U in the range of 4-6 eV, allowing the determination of an improved band gap and related bulk properties [77]. We see that our self-determined U is 4.90 eV, which is within the range and is in good agreement with the experimental data shown in Table 5. From Figure 5, we find the Cr 3d and O 2p orbital levels are aligned in two bands with a small gap below 0 eV (valence band maximum, VBM). The band structure calculation in this work follows the default high-symmetry point path (F→Γ→Z) within the first Brillouin zone (BZ) in reciprocal space. An indirect band gap of Cr_2O_3 is 3.11 eV was found, which is in a good agreement with the CVD experimental measurement [75], while the direct band gap for the Γ→Γ optical transition was found to be 3.41 eV, close to that found by photoemission measurement [74] and optical absorption data [72, 73]. Further comparison of the PBE+U calculations with empirical U parameters has been provided in Figure S4 of the supplemental information.

Researchers have devoted considerable effort to correcting the self-interaction energy error by treating only the spurious error component within their calculation method/functional. Based on our work here, however, the correction can have a physical meaning to correct the orbitals. The simplest strategy is to use the DFT+U method, which adds an on-site repulsive potential U for the localized d and f orbitals of solids to cancel the self-interaction energy [79, 80]. Even with this simple method, however, the choice of the U parameter for the correction to match the experimentally reported data is primarily semi-empirical and still leads to errors in band structure calculations, especially in defect-state calculations. In fact, defect-state levels in the band structure arise from the host in the BZ and the area correlated with the excited states of the band structure. A calculation method that closely describes the band structure may not be adequate to correctly reflect the defect states, especially the deep-level states. Therefore, we must carefully determine the U parameters for further defect-state studies.

3. Electronic structure of Kagome Staircase compounds ($Co_3V_2O_8$)

$Co_3V_2O_8$ (CVO) is a type of oxide from the kagome staircase vanadium oxide family [81-87], and has an orthorhombic lattice with symmetry group *Cmca*. CVO has been reported to possess temperature-dependent ferromagnetic behavior and has an incommensurate spin structure and multiferroic behavior. In the literature, optical studies on CVO have used DFT band structure calculations based on the LDA.

However, those studies further determined that no discrepancy exists between experimental observations and LDA or LDA+U calculations with the improper choice of U parameter for the 3d orbitals of Co and V [88-90]. Moreover, the electronic fundamental band gap for CVO is approximately 0.4 eV, showing semi-metallic behavior through recent experiments using X-ray absorption spectroscopy (XAS) and soft X-ray emission spectroscopy (XES) [90]. Empirically tuned LDA+U calculations were also performed but did not match the experiment. Therefore, it is necessary to facilitate a preliminary test on such an electronic band structure in a ferromagnetic spin lattice. In the meanwhile, we have carried out an investigation with standard PBE+U calculations with different input U parameters, as shown in Figure S5 of the supplemental information.

To obtain an improved band structure for the crystal structure of ferromagnetic CVO, we need to predict the on-site Hubbard U parameters of the Co 3d, V 3d, and O 2p orbitals through the new method introduced earlier. As shown in Table 6, we illustrate our predicted U together with the fractional coordinates of different sites. We see that U varies obviously for the same atomic species sitting at different sites. From Table 6, we see that the fractional coordinates of the atomic sites are almost the same and that the lattice parameters of the crystal structure exhibit a relative error of ~2%. In particular, our calculated band gap is in agreement with the experimentally determined value within acceptable deviation. The process of determining the on-site Hubbard U is illustrated in Figure 6.

Figure 7 (a) shows the calculated band structure of CVO based on DFT+U calculations, with U predicted by our method. This method gives an indirect band gap of 0.498 eV from Γ to Y. The optical transition gap from Γ to Γ is 0.792 eV, while the transition gap from Y to Y is 0.534 eV. Upon further analysis of the partial density of states (PDOS) in Figure 7 (b), the conduction band edge is dominantly determined by the V sites, which actually contribute the spin-up empty d-orbital levels, while the valence band is actually hybridized by the p and d orbitals of the O and Co sites, respectively. This is consistent with recent observations by combined XAS and XES analysis in the study by Laverock et al. [90].

4. The feasibility of using hybrid-functional DFT to compute U

As introduced in the Calculation Method and Settings section, the choice of the Hubbard U parameter in DFT+U calculations is determined by $U_{in,I}$ following the conditions of Eq. (11). This does not constrain the choice of functional implemented in the iterative determination process. In this work, most of our DFT+U calculations are based a local exchange-correlation (XC) functional, such as the LDA/GGA method. Now, we consider hybrid-DFT (non-local XC), which implements the XC functional in the form of a combination of partial HF exchange (α_{HF}) by short-range screening (ω or k_{TF}), together with a local correlation given by LDA/GGA. To validate this method, it is necessary to determine its feasibility. Therefore, its feasibility is an intriguing question that needs to be explored.

As indicated in Figure 8, our method confirms that it allows all types of applicable XC functionals to participate in the U computations to suggest the parameters to be used in DFT+U. We have provided the U determination results using sX-LDA, HSE03, B3LYP, and PBE0 (i.e., hybrid-PBE) on the effective U parameters of the $3d^{10}$ orbital of Zn in ZnO. α_{HF} and the screening length parameters k_{TF} were set to the default values. U converged at 4.5 eV using sX-LDA, which is a lower value than that given by the other functionals. This may due to relatively large α_{HF} (100% HF exchange) and LDA correlation, as well as k_{TF} using the Thomas-Fermi screening model on a nearly free electron gas [13, 14, 36]. B3LYP shows a larger determined U of approximately 7.7 eV, as it mixes 25% HF, LDA, and GGA exchange-correlation together. HSE03 and hybrid-PBE provide U values similar to that found by plain PBE. This arises because both HSE03 and hybrid-PBE use PBE correlation but replace the PBE exchange with 25% HF exchange.

In Figure 8, we also find that at relatively small U, from 0 to 4 eV, the potential minimization process returns a drastic convergence oscillation among four non-local XC functionals. The difference begins converging starting at 4-5 eV. This indicates that the choice of the small U for metal oxides normally induces the evident pseudo-charge effect, leading to obvious deviations from the true orbital eigenvalues.

Although the functionals have different convergence behavior when searching for the suitable input value of U, the results are all similar and are located within a reasonable range. From this, we can see that U in the DFT+U method has a physical property and meaning that is valid beyond the choice of functional, regardless of the choice of local XC functionals (LDA/GGA) or non-local XC functionals (hybrid-DFT e.g., sX-LDA, HSE, B3LYP, etc.).

5. Hybrid-DFT+U_{eff}^{hybrid}

Recently, Ivady and Gali et al. theoretically proved the unification of hybrid-DFT and DFT+U for treating localized orbitals [44, 45]. They justifiably added a DFT+U-like on-site potential correction in hybrid-DFT, where the additional total energy term is

$$\Delta E_X^{PBE0}\left[\left\{n_m^\sigma\right\}\right]=\frac{\alpha_{HF}\left(F^0-J^0\right)}{2}\sum_{m,\sigma}\left[n_m^\sigma-\left(n_m^\sigma\right)^2\right], \tag{28}$$

where the occupation matrix n_m^σ is the same as the one used in DFT+U, F^0 is the Slater integral of the Coulomb interaction, and $J^0=(F^2+F^4)/14$, where $F^4/F^2\approx0.625$. Thus, the relationship between the two equivalent contributions to the Hubbard U_{eff} is

$$\begin{cases}U_{eff}^{DFT+U}=U-J\\ U_{eff}^{hybrid}=\alpha_{HF}\left(F^0-J^0\right)\end{cases}, \tag{29}$$

The difference between the two Hubbard parameters is defined as the strength of the additional correction and potential w in the forms of

$$w=-\left(U_{eff}^{hybrid}-U_{eff}^{DFT+U}\right), \tag{30}$$

In this way, the original Hubbard U_{eff} potential is replaced by a multiplicative operator of α_{HF} and Slater integrals (F^0 and J^0). The import of w fulfills the gKT conditions in hybrid-DFT+U_w calculations. We compared the w values determined by different hybrid density functional methods with our method in this work, shown in Table 7. We found repulsive strengths ($w>0$) using the default sX-LDA and PBE0 functionals that are very similar with close magnitude. However, the range-separated default HSE03 functional gives an attractive strength ($w<0$) that is has a smaller magnitude than that given by B3LYP.

We applied U_{eff}^{hybrid}, which was self-consistently determined by the chosen hybrid density functional method, to hybrid-DFT calculations. The sX-LDA and HSE03 functionals were selected for comparison. To illustrate the improved performance upon adding U, the α_{HF} of both functionals was set to the default value, 100% for sX-LDA and 25% for HSE03. The Thomas-Fermi screening length k_{TF} was adjusted to 0.76 $Bohr^{-1}$, which is the default value for sX-LDA derived from the electron-gas limit used in LDA/GGA. For HSE03, a similar parameter representing the short-range screening length ω was set to 0.158 $Bohr^{-1}$.

Figure 9 (a) shows the band structure and TDOS of ZnO calculated by sX-LDA using the U determined from Figure 8 (a), and the U for the 2p orbitals of O was also computed using sX-LDA to give a value of U_p=4.15 eV. All the determined values were lower than the ones determined by plain PBE for PBE+U calculations, which may be because the full or partial percentage of HF exchange involved in the density matrix determination of the orbital

occupancies is different than that in LDA/GGA. The default sX-LDA functional gives a direct band gap of 3.366 eV, which is close to the result of 3.41 eV from the plain sX-LDA calculation with k_{TF} manually adjusted to k_{TF}=2.27 A^{-1} (i.e., 1.20 $Bohr^{-1}$), as suggested by one of our collaborators, Robertson et al. [13, 14, 36]. Meanwhile, compared with the ACBN0 method of Agapito et al. (2.91 eV) [91], our result shows a more obvious improvement.

In general, our values are still slightly lower than the reported experimental value of 3.44 eV [92]. The occupied 3d level (t_{2g} component) of Zn ranges from 6.5 eV to 9 eV below the VBM, which is similar to the range calculated by Robertson et al. [36] and that given by experiments [92]. If we further use the U parameters determined by default, combined with the k_{TF}=2.27 A^{-1} screened sX-LDA, the band structure calculation return a band gap of 3.848 eV, and the 3d level ranges from 6.3 eV to 9 eV below the VBM. Therefore, accurate calculation, compared to experimental data, is sensitive to the value of α_{HF}, k_{TF} and U.

Another functional, HSE03, is shown in Figure 9 (b). The band structure and TDOS calculations show a direct band gap of 3.616 eV using the default α_{HF} and ω of HSE03, which is slightly higher than the reported value of 3.44 eV [92]. The 3d level is downshifted from 8.5 eV to 11.3 eV below the VBM. As shown in Table 7, the implementation of U on the orbitals shows an improvement compared with using plain HSE03 with its default settings, as done by Oba et al. [37]. The default settings of α_{HF}=25% and ω=0.158 $Bohr^{-1}$ of plain HSE03 give a direct band gap of 2.49 eV, and our method improves this by 1.13 eV. For the plain HSE03 calculation, the improvement will be only achieved with the α_{HF} manually tuned to 37.5% to obtain 3.43 eV [37].

From Figure 9, we see that the hybrid-DFT+U calculations still lead to some deviations from the experimental data. Thus, we have the following concerns about using this combination. First, the remaining small difference arises because hybrid-DFT has already been reported to improve the band gap of solids using the pre-set parameters, such as α_{HF} and the short-range electron-gas screening length (e.g., k_{TF} in sX-LDA or ω in HSE). Adding U will disturb the previous settings in hybrid-DFT that were originally fit to experimental data. Second, if hybrid-DFT+U is used in a self-consistently manner, many parameters need to be self-consistently determined, rather than the U parameter only. This means that it is necessary to consider α_{HF}, k_{TF}, and U as global parameters to be self-consistently computed for future hybrid-DFT+U calculations.

We finally analyze possible contributions from the PPs and screening functions in the hybrid-functional calculations, especially in the sX-LDA method. This may be an alternative way to conduct error analysis of the computations. First, the choice of functional and its transferability to PP generation is another possible source influencing the electronic structures in hybrid-functional calculations (note: here, we only consider the norm-conserving PP). This arises because the PBE functional is commonly used for GGA-based norm-conserving PPs in the atomic limit to align with the homogeneous electron-gas limit, where k_{TF} is given as 0.76 $Bohr^{-1}$. Figure 10 shows that sX-LDA with a norm-conserving PP generated based on the pure HF functional gives a band gap for ZnO of 3.646 eV. This seems to be more consistent with the framework of screened HF theory (sX). However, details in the band structure do not fully agree with experimental data. The t_{2g} component of the Zn 3d orbitals (occupied 3d) ranges from E_V-9.2~E_V-10.4 eV below the VBM (E_V=0 for VBM), while E_V-7.0 eV in the experiment.

Another complementary effect on the electronic structure calculation is the screening function multiplying the pure exchange energy functional. The sX-LDA functional was recently developed based on the prototype of Kleinman and Bylander (KB) [35]. It uses 100% pure HF exchange but is screened by the Thomas-Fermi model and keeps the original LDA correlation. The non-local sX density functional is given as:

$$E^{sX}[\rho] = E_x[\rho]F[\gamma] = \left[-\frac{3}{2}\left(\frac{3}{\pi}\right)^{1/3} \rho^{4/3}(\mathbf{r}) \right] F[\gamma], \tag{31}$$

The entire form of the KB screening function is

$$F[\gamma] = 1 - \frac{4}{3}\tan^{-1}\left(\frac{2}{\gamma}\right) - \frac{\gamma^2}{6}\left[1 - \left(\frac{\gamma^2}{4} + 3\right)\ln\left(1 + \frac{4}{\gamma^2}\right)\right], \tag{32}$$

where $\gamma = K_S/k_{TF}$ is Thomas-Fermi screening parameter. Here, we replace the original KB screening function F[γ] by a modified form (KB-Mod) based on the original KB function:

$$F^{KB-Mod}[\gamma] = F[\gamma] - \frac{1}{2}\tan^{-1}\left(\frac{2}{\gamma}\right), \tag{33}$$

The band gap of ZnO when k_{TF}=0.76 Bohr^{-1} is 3.430 eV, as shown in Figure 10, which is improved by 1.8 eV compared with that given by the original sX-LDA with k_{TF}=0.76 Bohr^{-1}. However, the O 2p orbital levels at the top of the valence band are slightly different from the results in Figure 9. Meanwhile, the Zn 3d occupied levels are shown to start from E_V-9.7~E_V-10.7 eV below the VBM (E_V=0 for VBM). Moreover, the modification of F[γ] is sensitive to the change in electronic structure, as shown in Figure 11. Therefore, it is desirable to take these additional two factors into account for further non-empirical sX-LDA calculations to develop more advanced hybrid density functional methods [39, 40, 43].

Although our method shows some improvements to hybrid-DFT, this still does not guarantee the optimal strategy for further computational applications. As stated by Robertson et al. [36], further comparison concerning the formation enthalpy and defect levels is needed. Meanwhile, the development of non-linear core-corrected PPs is needed in follow-up calculations [69]. This is being undertaken in our upcoming work.

Summary

In summary, we proposed a pseudo-charge potential model within the CLR framework to solve the on-site effective screened Coulomb potential for cations and anions in solids with either fully occupied (closed shell) or partially occupied (open shell) orbitals. This model can not only quickly give electronic structures of the eigen-bulk properties but also provide satisfactory native defect levels of bulk or low dimensional structures. This method helps propel our research and guides the discovery of next-generation high-throughput electronic engineering materials, which are formed or synthesized under extreme physical or chemical environments, at a faster pace.

Acknowledgements

This work is supported by the Natural Science Foundation of China (NSFC) for the Young Scientist grant (Grant No. NSFC 11504309), the initial start-up grant support from the

Department General Research Fund (Dept. GRF) from ABCT at Hong Kong Polytechnic University, and the Early Career Scheme (ECS) Fund (Grant No. PolyU 253026/16P) from the Research Grant Council (RGC) in Hong Kong.

Table 1. The Closed d/f shell charge responses on some typical solids estimated by conventional linear response (CLR) are demonstrated. In the CLR calculation demonstration, we set the Lagrange multiplier type orbital perturbation (α), with energy scale of α=0.05 eV.

Charge Response by α Perturbation on Closed d/f	
α=0.05 eV on d/f shell	CLR
Cu	1.85E-03
Zn	7.41E-04
Cu_2O	5.88E-03
ZnO	1.52E-03
ZnS	7.65E-04
CdO	1.53E-03
CdS	8.96E-04
GaN	3.78E-04
GaP	2.17E-04
GaAs	1.49E-04
GaSb	1.05E-04
Lu_2O_3	1.41E-03

Table 2. Summary of the comparison of some Hubbard U parameters on the d/f orbital based solids calculated by CLR and new method in this work. The CLR has evidently shown the overestimation on the U for closed-shell solids, and underestimations on some open-shell solids. (am-ZnO denotes the amorphous ZnO with density closed to the experimental reported value. U is the averaged value used in the 64-atom simple cubic type supercell.)

	U on d/f done by this work	
Unit: (eV)	CLR	new method
Sc	0.7	3.2
Fe_bcc	1.8	2.1
Fe_fcc	1.7	1.6
Ni	0.2	0.2
Cu	27.1	8.3
Zn	67.5	10.8
Y	-0.02	5.1
Er	10.0	11.2
Gd	-1.8	9.8
Lu	32.9	11.5
Ni_2P	14.7	4.9
Cu_2O	8.5	6.3
ZnO	33.0	11.2
RS-ZnO	39.7	10.3
am-ZnO	38.5	12.8
ZnS	65.4	13.1
CdO	32.6	10.1
CdS	55.8	13.2
GaN	132.2	17.9
GaP	230.5	17.5
GaAs	335.2	16.2
GaSb	474.3	15.8
Lu_2O_3	35.4	14.0

Table 3. Comparison of the calculated PBE+U(scf) for binary filled-shell compounds to the experimental results. The experimental band gaps refer to those at 0 K (Refs. [13, 92-99]).

Compound	*U*d (scf) (eV)	*U*p (scf) (eV)	Lattice (Å)	Exp. Lattice (Å)	*E*g (eV)	Exp. *E*g (eV)	$E_{d/f}$ (eV)	Exp. $E_{d/f}$ (eV)
ZnO (hex)	11.238	6.502	3.248/5.216	3.249/5.205	3.441	3.44	-7.5	-7.3
ZnS (cub)	13.083	5.174	5.470	5.409	3.846	3.8	-10.7	
CdO (cub)	10.102	6.862	4.704	4.695	1.379/ 2.459	2.3(dir)	-7.8	
CdS (cub)	13.210	5.061	5.893	5.832	2.652	2.4	-12.3	
GaN (cub)	17.878	6.866	4.552	4.540	3.534	3.504	-21.2	-22.2
GaP (cub)	17.513	4.802	5.567	5.450	2.491	2.32	-22.6	
GaAs (cub)	16.205	4.779	5.717	5.653	1.755	1.519	-22.8	-22
Cu_2O	6.850	13.122	4.276	4.270	2.159	2.17	-4.5 to 0	
CuO (AFM)	6.361	4.322	4.558/3.644/ 5.207	4.653/3.410/ 5.108	1.681	1.7	-9.5 to -2	
Lu_2O_3 (hex)	13.976	5.467	3.604/5.812		5.584	5.5	-6.8	
Lu_2O_3 (cub)	12.307	5.497	10.472	10.391	5.528	5.5	-6.0	-5.8
CZTS-KS	5.963 (Cu) /6.820 (Zn)	5.544	5.467 /10.934	a=b=5.427 /c=10.872	1.404	1.4-1.5		
CZTS-WZ	5.065 (Cu) /5.942 (Zn)	5.441	7.703 /6.331	c=6.4	1.440	1.4-1.5		

Table 4. Standard results of current PBE+U_{scf} calculations for benchmarking with other calculation methods in different packages.

Benchmark		*a* (Å)	*c* (Å)	*E*g (eV)	E_{3d} (eV)	Δ*H*f (eV)	*V*o (O-poor)	Refs
VASP	PBE_PAW_U	3.148	5.074	1.51	-6.0	-3.50	3.72	[100]
	PAW_HSE	3.261	5.225	2.49	-5.8	-3.01	0.96	[37]
	PAW_HSE_(0.375)	3.249	5.196	3.43	-6.4	-3.13	1.01	[37]
	PAW_GW			3.34				[101]
CASTEP	PBE+NoNLCC	3.286	5.299	0.90	-4.8	-2.93		[102, 103]
	PBE+NLCC	3.278	5.301	1.04	-4.0	-3.20		[this work]
	sX	3.267	5.245	3.41	-7.0	-3.31	0.85	[102, 103]
	PBE+U(scf)+NLCC	3.248	5.216	3.441	-7.53	-3.70	0.963	[this work]
Exp.	Exp. (1)	3.242	5.188	3.44	-7.5	-3.63		[104, 105]
	Exp. (2)	3.249	5.205	3.44	-7.3			[106, 107]

Table 5. Experimental and calculated properties of Cr_2O_3 with comparison. (MC: Mosey and Carter; fixed: without any cell geometry parameter relaxation)

	sX[76]	MC (+U)[77]	this work	Exp.[72-75]
a (Å)	4.988 (fixed)	5.052	5.079	4.961
c (Å)	13.667 (fixed)	13.853	13.498	13.599
V(Å^3)	294.56 (fixed)	306.220	301.556	287.98
Eg (indirect) (eV)	3.310	2.900	3.110	2.98-3.09, 3.3, 3.4-3.5
Eg (direct) (eV)	3.900		3.412	
μ_B	3.52	2.900	3.744	3.8

Table 6. Summary of the standard PBE+U_{scf} calculated $Co_3V_2O_8$ (ferromagnetic) crystal structure and comparisons with experimental reported data[90, 108]. The predicted on-site Hubbard U parameters are also provided.

	x (exp)	x (calc.)	y (exp)	y (calc.)	z (exp)	z (calc.)	U_d or U_p		exp.	calc.
Co-1	0.000	0.000	0.000	0.000	0.000	0.000	6.28	a (Å)	6.030	6.152
Co-2	0.250	0.250	0.133	0.131	0.250	0.250	4.04	b (Å)	11.486	11.713
V	0.000	0.000	0.377	0.376	0.120	0.116	6.38	c (Å)	8.312	8.472
O-1	0.000	0.000	0.250	0.248	0.229	0.227	6.24	Eg (eV)	0.4	0.498
O-2	0.000	0.000	0.001	0.000	0.245	0.248	3.93			
O-3	0.270	0.266	0.119	0.117	0.998	0.993	4.27			

Table 7. Summary of the strength of additional correction and potential follows the theory of hybrid-DFT+U by Ivady et al[45].

Functional	sX-LDA	HSE03	B3LYP	PBE0
w	1.173	-0.781	-2.171	0.619

Figure 1.

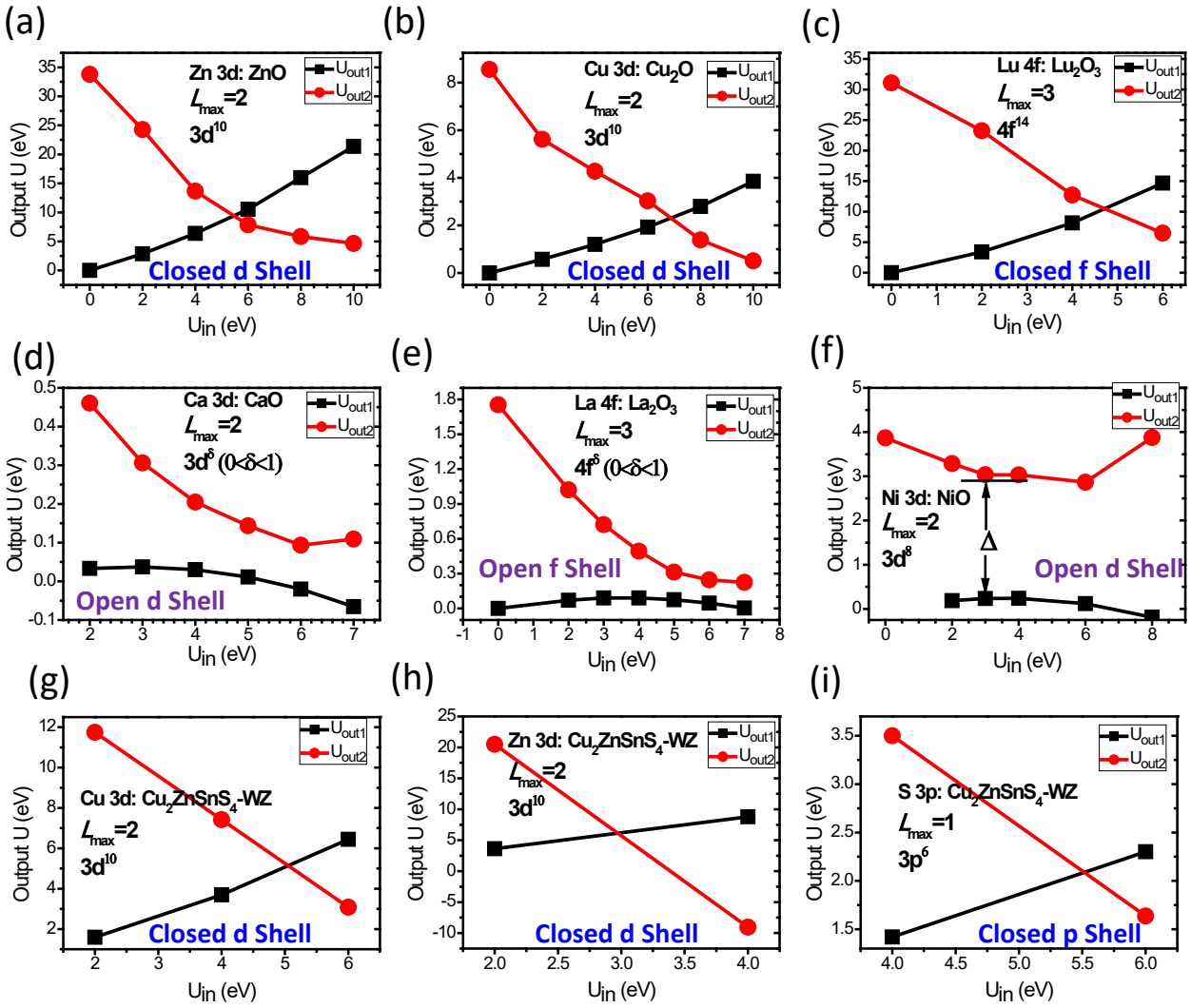

Figure 1. Obtained values of U_{out1} and U_{out2} for fully occupied orbitals of (a) ZnO, (b) Cu_2O (c) Lu_2O_3, and (g)-(i) for CZTS. The crossover feature indicates $|U_{out1} - U_{out2}| = 0$. This result contrasts with (d) CaO, (e) La_2O_3, and (f) NiO with partially occupied orbitals without crossover.

Figure 2.

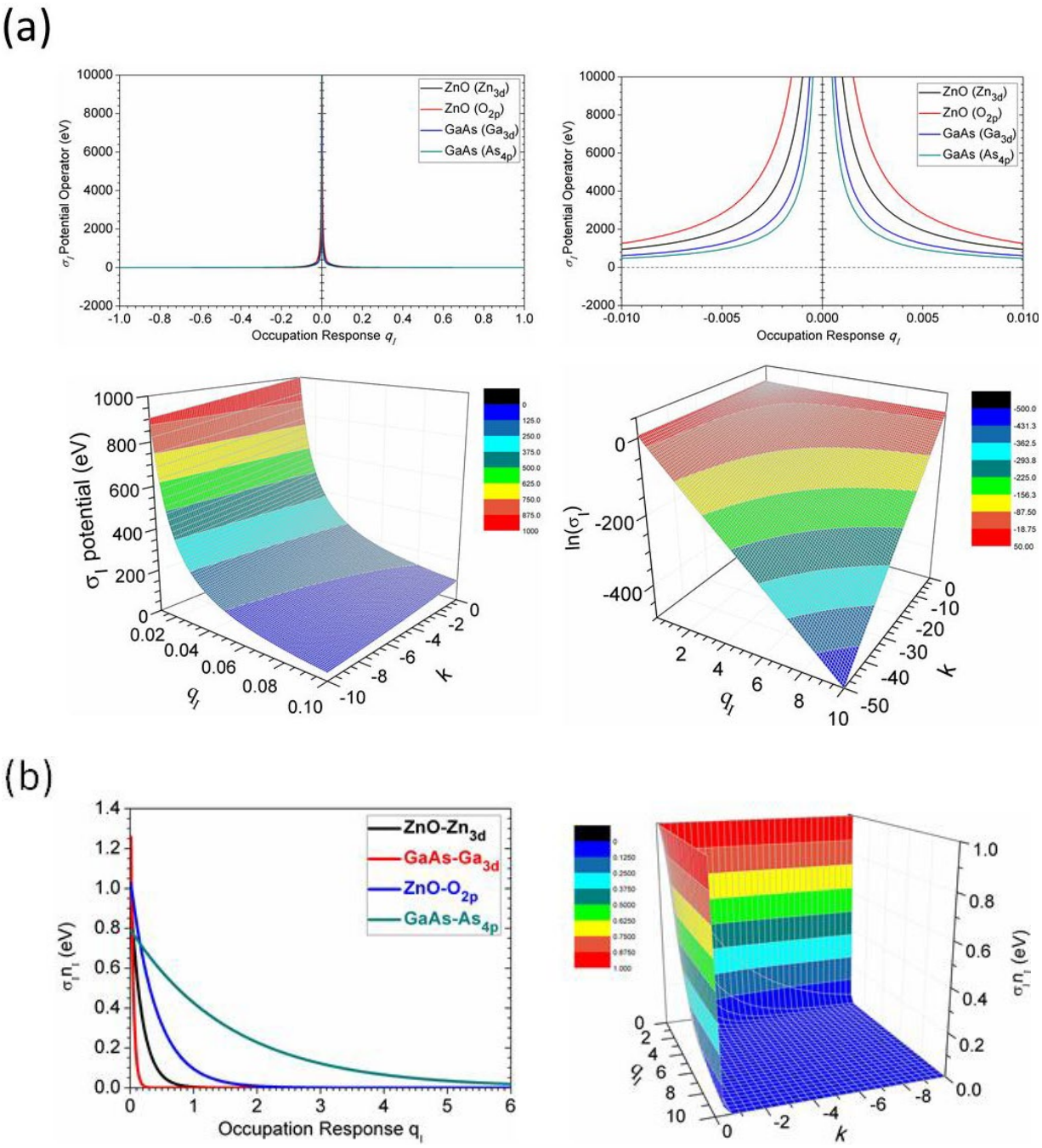

Figure 2. (a) The relationship between the self-consistently yielded potential operator σ_I and the on-site occupation response q_I. (b) The screening behavior of pseudo-charge induced potential with related to the response charge q_I.

Figure 3.

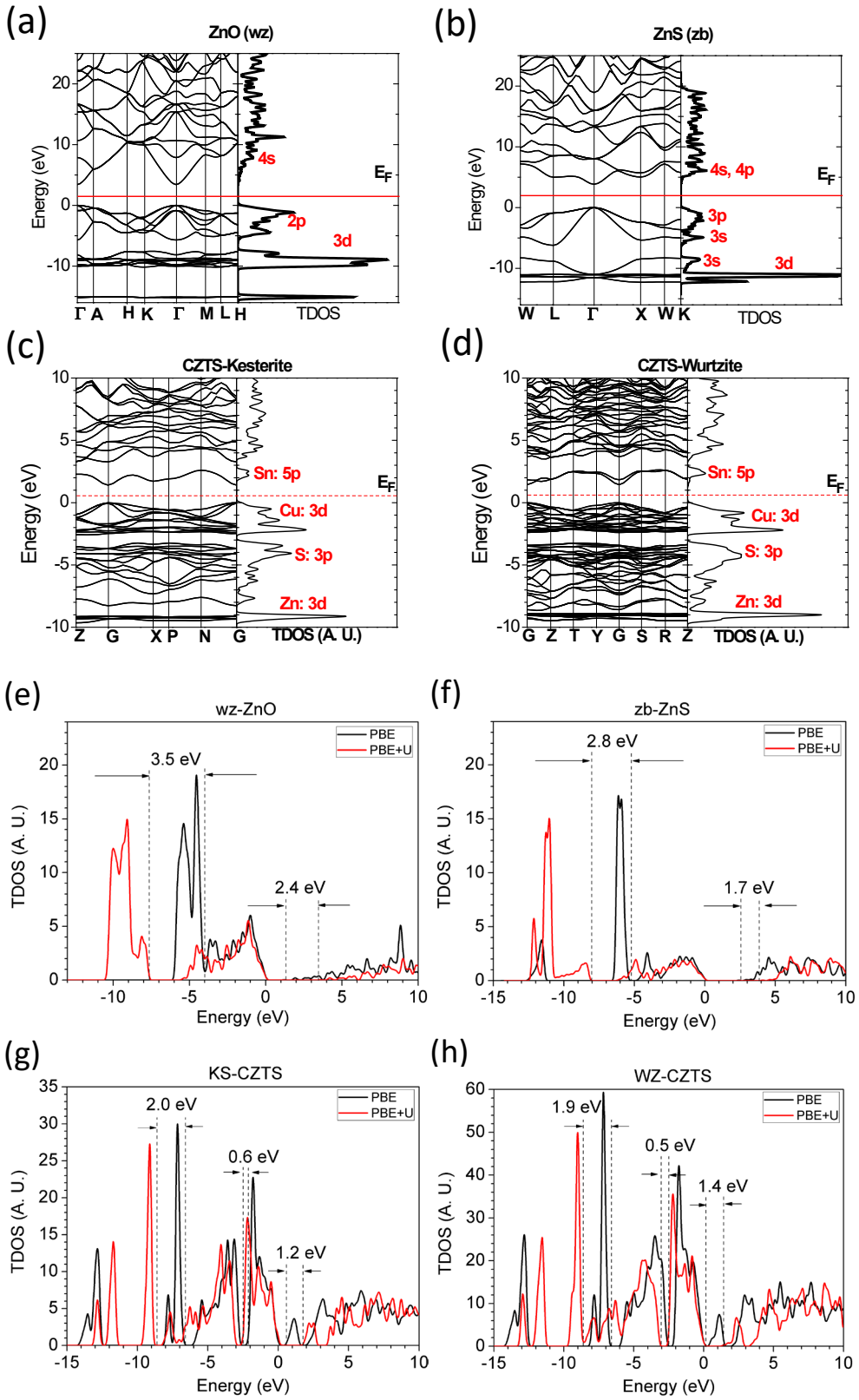

Figure 3. Standard PBE+U calculations on band structures of ZnO in the WZ phase (a) and ZnS in the zincblende phase (b). (c) CZTS in KS lattice and (d) a hexagonal WZ-like lattice.

The DOS comparisons are shown in (e), (f), (g) and (h) for wz-ZnO, zb-ZnS, KS-CZTS, and WZ-CZTS respectively.

Figure 4.

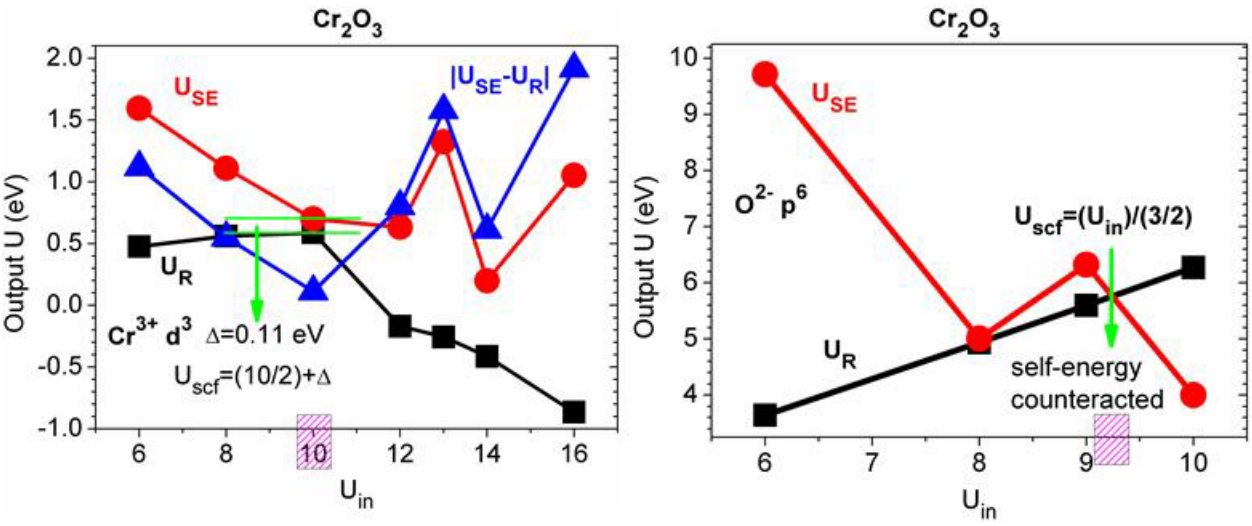

Figure 4. Obtained Hubbard projections of U_{out1} and U_{out2} for 3d orbitals of Cr^{3+} and 2p orbitals of O^{2-} in corundum Cr_2O_3 within G-type AFM phase.

Figure 5.

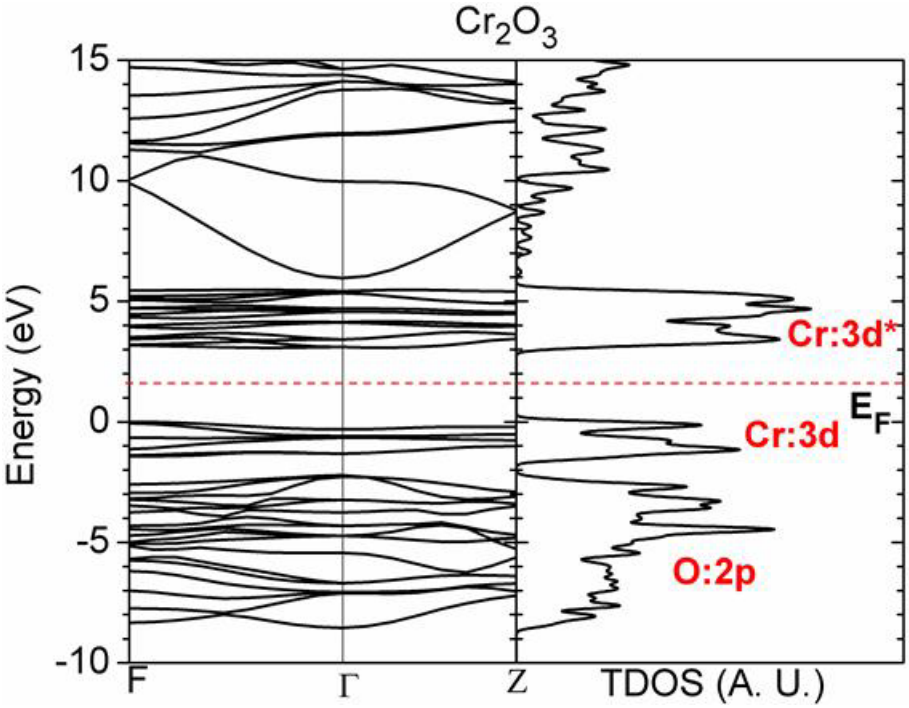

Figure 5. Band structure and TDOS of anti-ferromagnetic Cr2O3 in corundum lattice (in G-type AFM phase)

Figure 6.

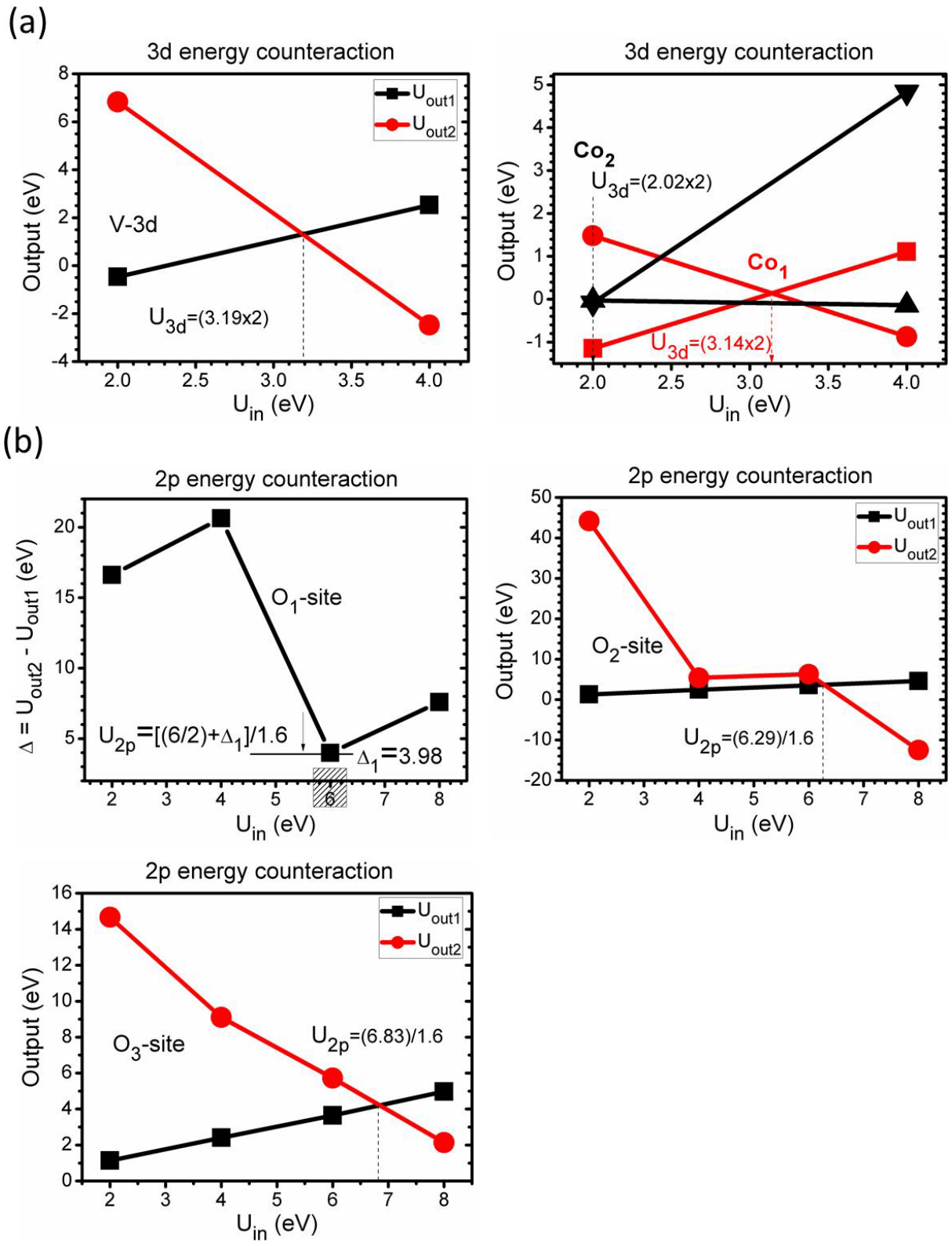

Figure 6. (a) Obtained Hubbard projections of U_{out1} and U_{out2} for 3d orbitals of V- and Co-sites (b) 2p orbitals of O in $Co_3V_2O_8$ in ferromagnetic lattice.

Figure 7.

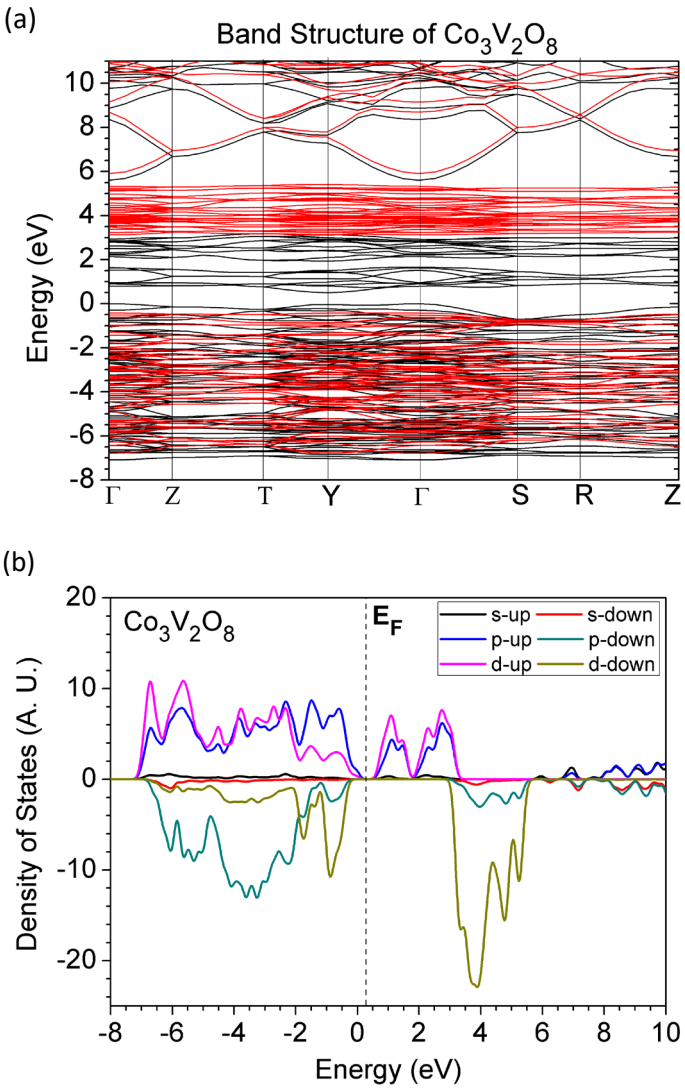

Figure 7. (a) Calculated band structure of CVO. (b) Density of states of CVO with s-, p-, and d- orbitals projected.

Figure 8.

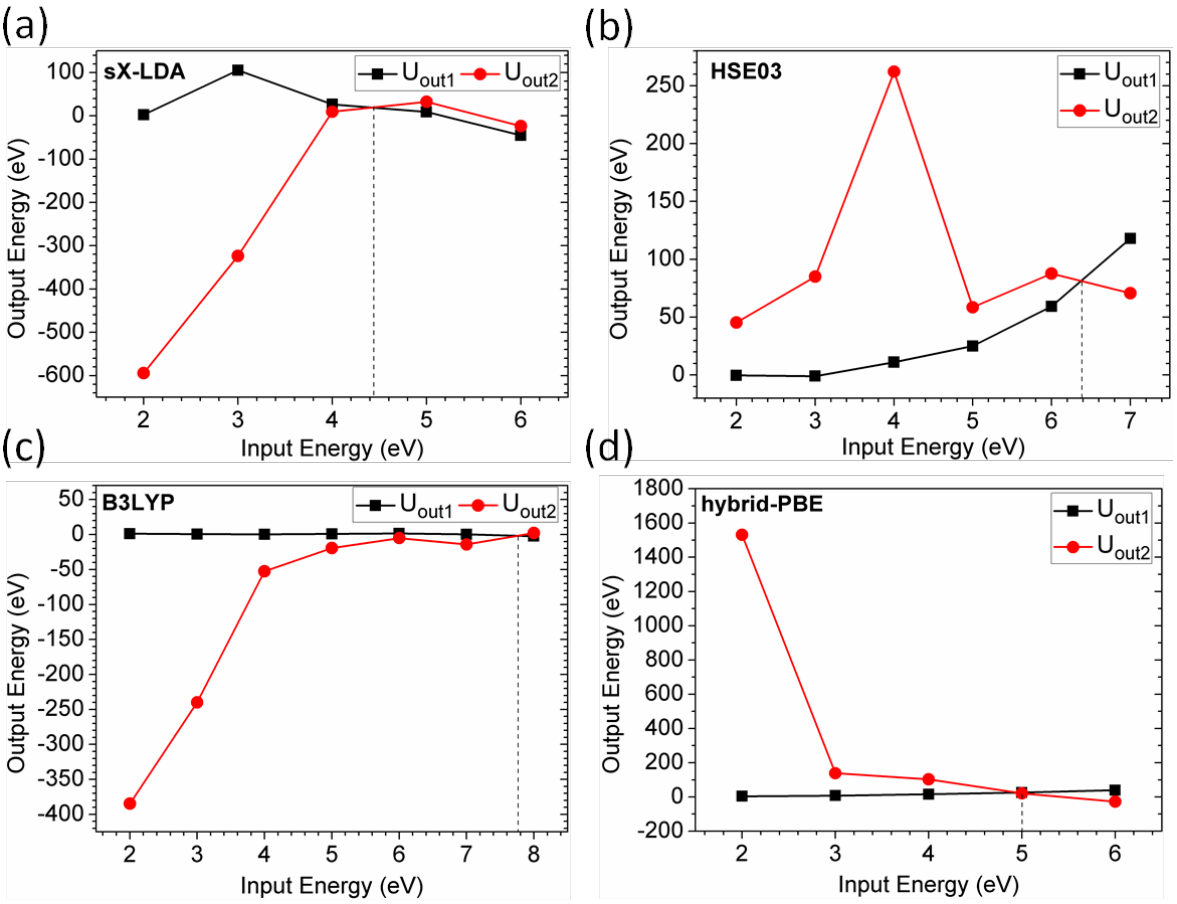

Figure 8. The U determination by using our method with non-local exchange-correlation functional (hybrid-DFT).

Figure 9.

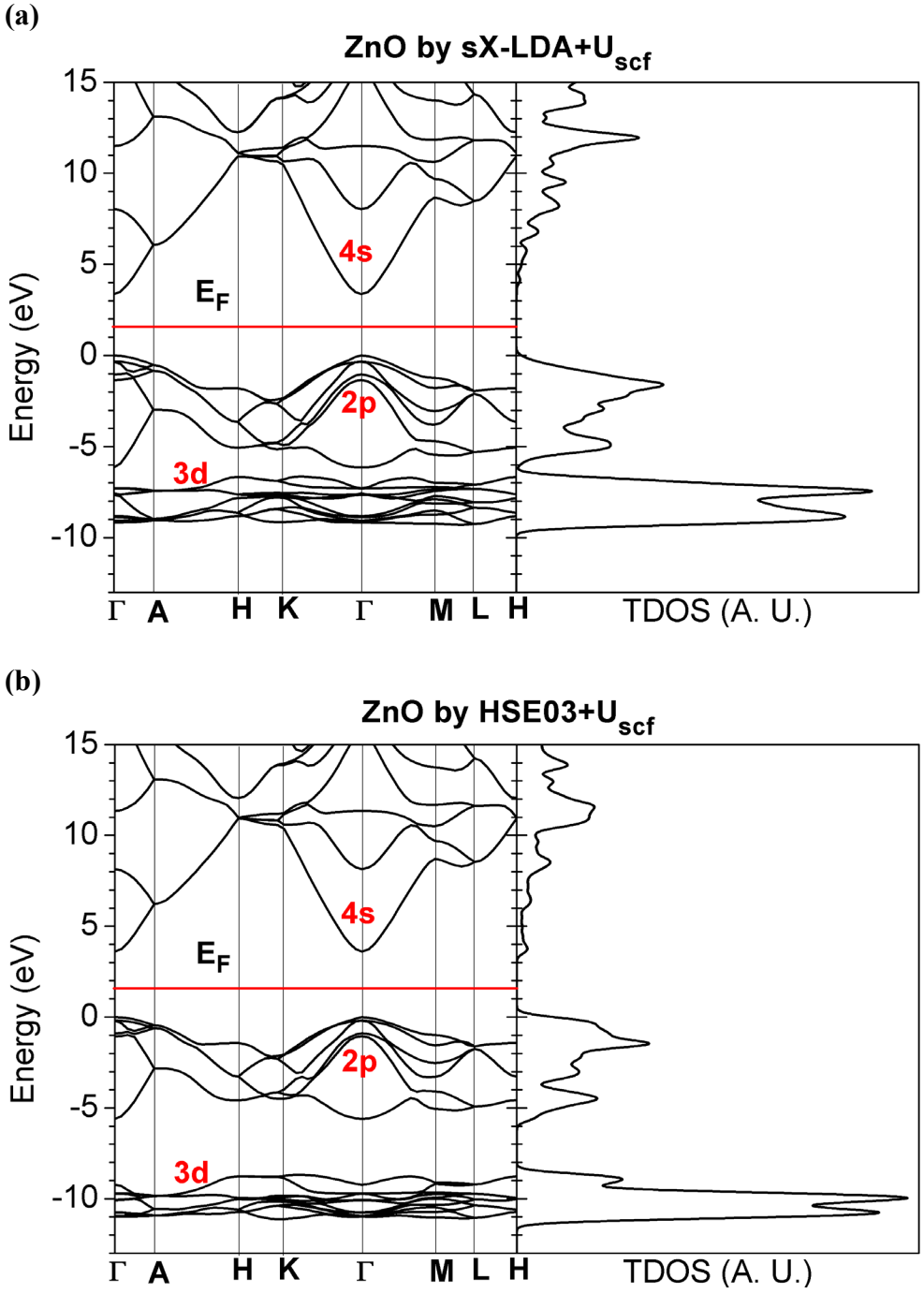

Figure 9. (a) Band structures and total density of states (TDOSs) of ZnO by (a) sX-LDA+U_{scf} and (b) HSE03+U_{scf} with self-consistently determined U parameters by default sX-LDA and HSE03 respectively. The U parameters for 3d of Zn and 2p of O have been both computed and implemented to the calculations.

Figure 10.

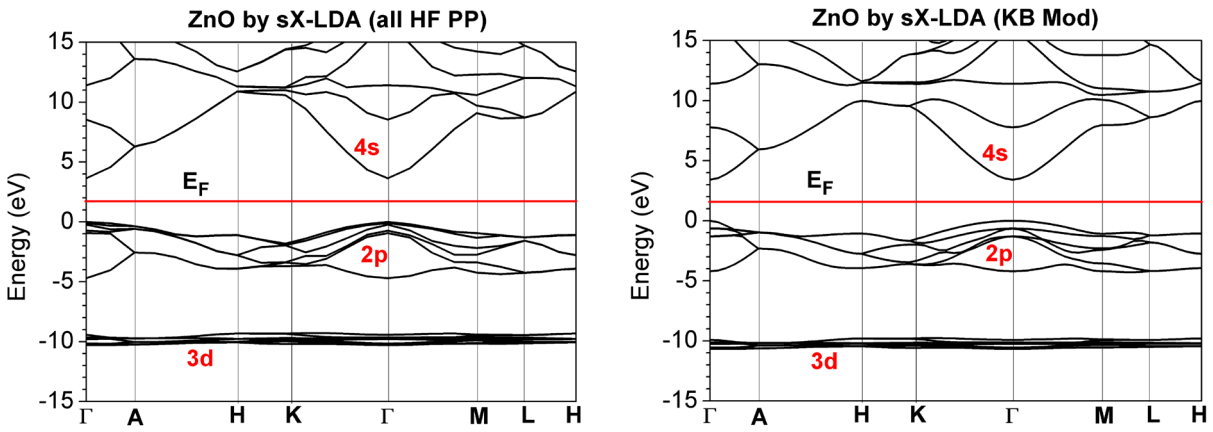

Figure 10. Band structures of ZnO by sX-LDA with pseudopotentials generated based on pure HF functional (left), and modified Kleinman-Bylander (KB Mod) screening function. Note the Thomas-Fermi screening length k_{TF} is all chosen to be the default 0.76 Bohr^{-1}.

Figure 11.

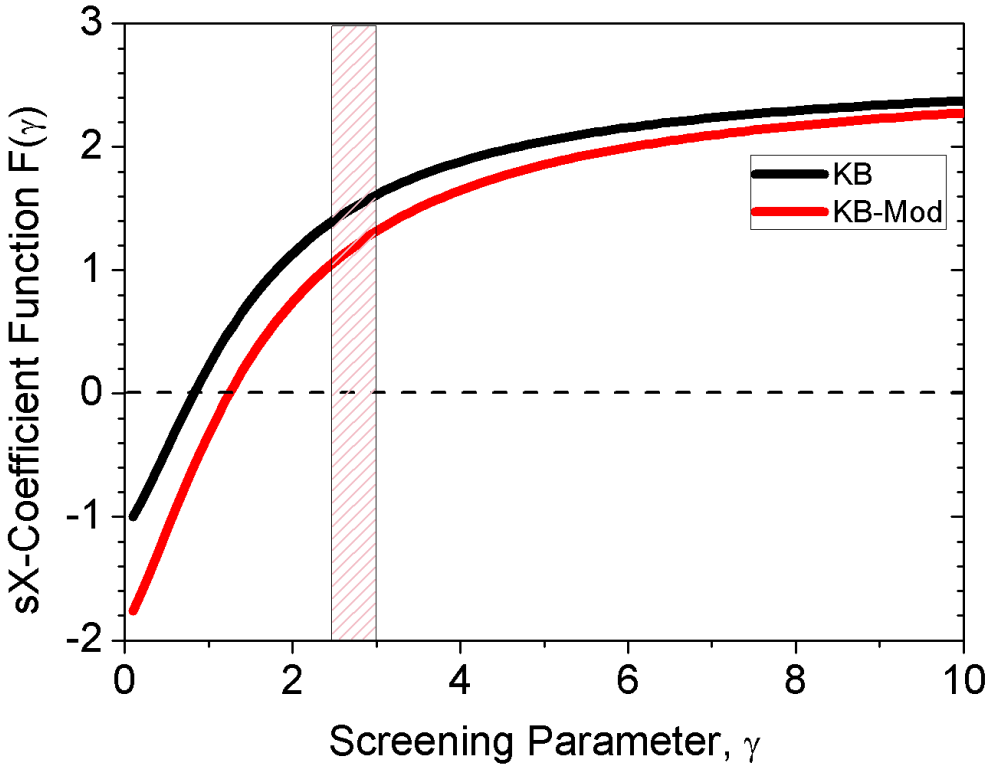

Figure 11. Screening functions with related to the parameter γ ($\gamma=K_S/k_{TF}$), based on Kleinman-Bylander original (KB) and modified (KB-Mod) forms. The pink shaded area denotes the extent of γ that is usually chosen for the transition metal based solids.

References

[1] I. A. Vladimir, F. Aryasetiawan, and A. I. Lichtenstein, J. Phys.: Condens. Matter **9**, 767 (1997).
[2] P. H. Dederichs, S. Blügel, R. Zeller, and H. Akai, Phys. Rev. Lett. **53**, 2512 (1984).
[3] A. K. McMahan, R. M. Martin, and S. Satpathy, Phys. Rev. B **38**, 6650 (1988).
[4] O. Gunnarsson, O. K. Andersen, O. Jepsen, and J. Zaanen, Phys. Rev. B **39**, 1708 (1989).
[5] M. S. Hybertsen, M. Schlüter, and N. E. Christensen, Phys. Rev. B **39**, 9028 (1989).
[6] V. I. Anisimov and O. Gunnarsson, Phys. Rev. B **43**, 7570 (1991).
[7] I. V. Solovyev, P. H. Dederichs, and V. I. Anisimov, Phys. Rev. B **50**, 16861 (1994).
[8] W. E. Pickett, S. C. Erwin, and E. C. Ethridge, Phys. Rev. B **58**, 1201 (1998).
[9] M. Cococcioni and S. de Gironcoli, Phys. Rev. B **71**, 035105 (2005).
[10] V. I. Anisimov, J. Zaanen, and O. K. Andersen, Phys. Rev. B **44**, 943 (1991).
[11] T. R. Paudel and W. R. L. Lambrecht, Phys. Rev. B **77**, 205202 (2008).
[12] A. Boonchun and W. R. L. Lambrecht, Phys. Rev. B **81**, 024103 (2010).
[13] S. J. Clark and J. Robertson, Phys. Rev. B **82**, 085208 (2010).
[14] S. J. Clark and J. Robertson, physica status solidi (b) **248**, 537 (2011).
[15] A. Janotti, D. Segev, and C. G. Van de Walle, Phys. Rev. B **74**, 045202 (2006).
[16] H. J. Kulik and N. Marzari, J. Chem. Phys. **133**, 114103 (2010).
[17] S.-j. Hu, S.-s. Yan, M.-w. Zhao, and L.-m. Mei, Phys. Rev. B **73**, 245205 (2006).
[18] S. Lany and A. Zunger, Phys. Rev. B **80**, 085202 (2009).
[19] S. Lany and A. Zunger, Phys. Rev. B **81**, 205209 (2010).
[20] A. Zunger and A. J. Freeman, Phys. Rev. B **16**, 2901 (1977).
[21] S. Lany and A. Zunger, Phys. Rev. B **80**, 085202 (2009).
[22] J. F. Janak, Phys. Rev. B **18**, 7165 (1978).
[23] A. Zunger and A. J. Freeman, Phys. Rev. B **16**, 2901 (1977).
[24] J. P. Perdew and A. Zunger, Phys. Rev. B **23**, 5048 (1981).
[25] A. D. Becke, J. Chem. Phys. **98**, 1372 (1993).
[26] C. Adamo and V. Barone, J. Chem. Phys. **110**, 6158 (1999).
[27] J. P. Perdew, M. Ernzerhof, and K. Burke, J. Chem. Phys. **105**, 9982 (1996).
[28] J. P. Perdew, K. Burke, and M. Ernzerhof, Phys. Rev. Lett. **77**, 3865 (1996).
[29] J. Paier, R. Hirschl, M. Marsman, and G. Kresse, J. Chem. Phys. **122**, 234102 (2005).
[30] J. Heyd, G. E. Scuseria, and M. Ernzerhof, J. Chem. Phys. **118**, 8207 (2003).
[31] J. Heyd and G. E. Scuseria, J. Chem. Phys. **120**, 7274 (2004).
[32] J. Heyd and G. E. Scuseria, J. Chem. Phys. **121**, 1187 (2004).
[33] J. Heyd, J. E. Peralta, G. E. Scuseria, and R. L. Martin, J. Chem. Phys. **123**, 174101 (2005).
[34] J. E. Peralta, J. Heyd, G. E. Scuseria, and R. L. Martin, Phys. Rev. B **74**, 073101 (2006).
[35] D. M. Bylander and L. Kleinman, Phys. Rev. B **41**, 7868 (1990).
[36] S. J. Clark, J. Robertson, S. Lany, and A. Zunger, Phys. Rev. B **81**, 115311 (2010).
[37] F. Oba, A. Togo, I. Tanaka, J. Paier, and G. Kresse, Phys. Rev. B **77**, 245202 (2008).
[38] S. Lany and A. Zunger, Phys. Rev. B **81**, 113201 (2010).
[39] J. H. Skone, M. Govoni, and G. Galli, Phys. Rev. B **93**, 235106 (2016).
[40] N. P. Brawand, M. Vörös, M. Govoni, and G. Galli, Physical Review X **6**, 041002 (2016).
[41] A. E. Raeber and B. M. Wong, J. Chem. Theory Comput. **11**, 2199 (2015).
[42] A. Prlj, B. F. E. Curchod, A. Fabrizio, L. Floryan, and C. Corminboeuf, The Journal of Physical Chemistry Letters **6**, 13 (2015).
[43] J. H. Skone, M. Govoni, and G. Galli, Phys. Rev. B **89**, 195112 (2014).

[44] V. Ivády, I. A. Abrikosov, E. Janzén, and A. Gali, Phys. Rev. B **87**, 205201 (2013).
[45] V. Ivády, R. Armiento, K. Szász, E. Janzén, A. Gali, and I. A. Abrikosov, Phys. Rev. B **90**, 035146 (2014).
[46] B. Himmetoglu, A. Floris, S. de Gironcoli, and M. Cococcioni, Int. J. Quantum. Chem. **114**, 14 (2014).
[47] A. N. Andriotis, R. M. Sheetz, and M. Menon, Phys. Rev. B **81**, 245103 (2010).
[48] A. N. Andriotis, G. Mpourmpakis, S. Lisenkov, R. M. Sheetz, and M. Menon, physica status solidi (b) **250**, 356 (2013).
[49] Y. Ma, M. Eremets, A. R. Oganov, Y. Xie, I. Trojan, S. Medvedev, A. O. Lyakhov, M. Valle, and V. Prakapenka, Nature **458**, 182 (2009).
[50] A. J. Mannix, et al., Science **350**, 1513 (2015).
[51] M. Aras and Ç. Kılıç, J. Chem. Phys. **141**, 044106 (2014).
[52] R. O. Jones, Rev. Mod. Phys. **87**, 897 (2015).
[53] B. Huang, J. Comput. Chem. **37**, 825 (2016).
[54] H. Jiang, P. Rinke, and M. Scheffler, Phys. Rev. B **86**, 125115 (2012).
[55] D.-K. Seo, Phys. Rev. B **76**, 033102 (2007).
[56] J. F. Janak, Phys. Rev. B **18**, 7165 (1978).
[57] H. J. Kulik, M. Cococcioni, D. A. Scherlis, and N. Marzari, Phys. Rev. Lett. **97**, 103001 (2006).
[58] L. Kleinman and D. M. Bylander, Phys. Rev. Lett. **48**, 1425 (1982).
[59] S. G. Louie, S. Froyen, and M. L. Cohen, Phys. Rev. B **26**, 1738 (1982).
[60] I. Grinberg, N. J. Ramer, and A. M. Rappe, Phys. Rev. B **62**, 2311 (2000).
[61] A. M. Rappe, K. M. Rabe, E. Kaxiras, and J. D. Joannopoulos, Phys. Rev. B **41**, 1227 (1990).
[62] I. A. Vladimir, F. Aryasetiawan, and A. I. Lichtenstein, J. Phys. Condens. Matter **9**, 767 (1997).
[63] N. Marzari, D. Vanderbilt, and M. C. Payne, Phys. Rev. Lett. **79**, 1337 (1997).
[64] L. Y. Lim, S. Lany, Y. J. Chang, E. Rotenberg, A. Zunger, and M. F. Toney, Phys. Rev. B **86**, 235113 (2012).
[65] X. Lu, Z. Zhuang, Q. Peng, and Y. Li, Chem. Commun. **47**, 3141 (2011).
[66] D. C. Reynolds, D. C. Look, B. Jogai, C. W. Litton, G. Cantwell, and W. C. Harsch, Phys. Rev. B **60**, 2340 (1999).
[67] W. Göpel, J. Pollmann, I. Ivanov, and B. Reihl, Phys. Rev. B **26**, 3144 (1982).
[68] X. Ma, Y. Wu, Y. Lv, and Y. Zhu, J. Phys. Chem. C **117**, 26029 (2013).
[69] B. Huang, R. Gillen, and J. Robertson, J. Phys. Chem. C **118**, 24248 (2014).
[70] C. H. Ahn, J. M. Triscone, and J. Mannhart, Nature **424**, 1015 (2003).
[71] G. Rollmann, A. Rohrbach, P. Entel, and J. Hafner, Phys. Rev. B **69**, 165107 (2004).
[72] A. Y. Dobin, W. Duan, and R. M. Wentzcovitch, Phys. Rev. B **62**, 11997 (2000).
[73] A. Y. Dobin and R. M. Wentzcovitch, J. Appl. Phys. **89**, 7201 (2001).
[74] R. Zimmermann, P. Steiner, and S. Hüfner, J. Electron Spectrosc **78**, 49 (1996).
[75] C.-S. Cheng, H. Gomi, and H. Sakata, physica status solidi (a) **155**, 417 (1996).
[76] Y. Guo, S. J. Clark, and J. Robertson, J. Phys.: Condens. Matter **24**, 325504 (2012).
[77] N. J. Mosey and E. A. Carter, Phys. Rev. B **76**, 155123 (2007).
[78] N. J. Mosey, P. Liao, and E. A. Carter, J. Chem. Phys. **129**, 014103 (2008).
[79] I. A. Vladimir, F. Aryasetiawan, and A. I. Lichtenstein, J. Phys.-Condens. Mat. **9**, 767 (1997).
[80] V. I. Anisimov, J. Zaanen, and O. K. Andersen, Phys. Rev. B **44**, 943 (1991).
[81] G. Lawes, et al., Phys. Rev. Lett. **95**, 087205 (2005).
[82] N. R. Wilson, O. A. Petrenko, and G. Balakrishnan, J. Phys.: Condens. Matter **19**, 145257 (2007).

[83] N. R. Wilson, O. A. Petrenko, and L. C. Chapon, Phys. Rev. B **75**, 094432 (2007).
[84] O. A. Petrenko, N. R. Wilson, G. Balakrishnan, D. M. Paul, and G. J. McIntyre, Phys. Rev. B **82**, 104409 (2010).
[85] N. R. Wilson, O. A. Petrenko, G. Balakrishnan, P. Manuel, and B. FÅk, J. Magn. Magn. Mater. **310**, 1334 (2007).
[86] G. Lawes, M. Kenzelmann, and C. Broholm, J. Phys.: Condens. Matter **20**, 434205 (2008).
[87] A. Kumarasiri and G. Lawes, Phys. Rev. B **84**, 064447 (2011).
[88] R. C. Rai, et al., Phys. Rev. B **74**, 235101 (2006).
[89] R. C. Rai, et al., Phys. Rev. B **76**, 174414 (2007).
[90] J. Laverock, B. Chen, A. R. H. Preston, K. E. Smith, N. R. Wilson, G. Balakrishnan, P. A. Glans, and J. H. Guo, Phys. Rev. B **87**, 125133 (2013).
[91] L. A. Agapito, S. Curtarolo, and M. Buongiorno Nardelli, Physical Review X **5**, 011006 (2015).
[92] R. T. Girard, O. Tjernberg, G. Chiaia, S. Söderholm, U. O. Karlsson, C. Wigren, H. Nylén, and I. Lindau, Surf. Sci. **373**, 409 (1997).
[93] K. Ozawa, K. Sawada, Y. Shirotori, and K. Edamoto, J. Phys.: Condens. Matter **17**, 1271 (2005).
[94] G. Seguini, E. Bonera, S. Spiga, G. Scarel, and M. Fanciulli, Appl. Phys. Lett. **85**, 5316 (2004).
[95] M. Heinemann, B. Eifert, and C. Heiliger, Phys. Rev. B **87**, 115111 (2013).
[96] J. S. Blakemore, J. Appl. Phys. **53**, R123 (1982).
[97] J. Ma, B. Garni, N. Perkins, W. L. O'Brien, T. F. Kuech, and M. G. Lagally, Appl. Phys. Lett. **69**, 3351 (1996).
[98] H. M. Upadhyaya and S. Chandra, J. Mater. Sci. **29**, 2734 (1994).
[99] D. Vogel, P. Krüger, and J. Pollmann, Phys. Rev. B **55**, 12836 (1997).
[100] A. Janotti and C. G. Van de Walle, Phys. Rev. B **76**, 165202 (2007).
[101] S. Lany and A. Zunger, Phys. Rev. B **81**, 113201 (2010).
[102] S. J. Clark, J. Robertson, S. Lany, and A. Zunger, Phys. Rev. B **81**, 115311 (2010).
[103] S. J. Clark and J. Robertson, Phys. Status Solidi B **248**, 537 (2011).
[104] D. C. Reynolds, D. C. Look, B. Jogai, C. W. Litton, G. Cantwell, and W. C. Harsch, Phys. Rev. B **60**, 2340 (1999).
[105] W. Göpel, J. Pollmann, I. Ivanov, and B. Reihl, Phys. Rev. B **26**, 3144 (1982).
[106] R. T. Girard, O. Tjernberg, G. Chiaia, S. Söderholm, U. O. Karlsson, C. Wigren, H. Nylén, and I. Lindau, Surf. Sci. **373**, 409 (1997).
[107] K. Ozawa, K. Sawada, Y. Shirotori, and K. Edamoto, J. Phys.-Condens. Mat. **17**, 1271 (2005).
[108] E. E. Sauerbrei, R. Faggiani, and C. Calvo, Acta Crystallographica Section B **29**, 2304 (1973).